Journal of Computational Physics 425 (2021) 109909

Contents lists available at ScienceDirect

Journal of Computational Physics

www.elsevier.com/locate/jcp

Design optimization of interconnected porous structures using extended triply periodic minimal surfaces

Ming Li [a], Liangchao Zhu [a], Jingzhi Li [b,*], Kai Zhang [c,*]

[a] State Key Laboratory of CAD&CG, Zhejiang University, Hangzhou, China
[b] Department of Mathematics, Southern University of Science and Technology, Shenzhen, China
[c] Department of Mathematics, Jilin University, Changchun, China

ARTICLE INFO

Article history:
Received 18 November 2018
Received in revised form 28 September 2020
Accepted 5 October 2020
Available online 9 October 2020

Keywords:
Extended triply periodic minimal surface
Anisotropic porous structures
Interconnected
Proper generalized decomposition
Design optimization

ABSTRACT

We propose an approach to design an optimized heterogeneous interconnected porous structure over a fixed macro-design mesh for performance optimization, which has seldom been addressed despite its extensive potential industrial applications. We achieve this by introducing the concept of the *extended triply periodic minimal surface* (ETPMS), defined by an implicit function with additional control parameters that can prescribe the element anisotropy and heterogeneity consistently. The control parameters are expressed as continuous explicit functions of spatial coordinates, and ultimately generate a porous structure with perfect geometric connections and fully interconnected pore networks. The modeling advantages of the ETPMS come at the cost of challenges in its efficient simulation and optimization owing to its large number of varied ETPMS elements and their geometric validity requirements. These issues are further resolved using a strategy of offline pre-computation; in particular, parametric homogenization and several carefully designed optimization techniques. The performance of the approach is demonstrated using a suite of three-dimensional benchmark examples.

1. Introduction

Porous structures appear extensively in natural objects such as bones, wood, cork, and bird beaks [1]. These structures manifest exceptional properties at relatively low densities, such as shock resistance [2], damping enhancement [3], and defect tolerance [4]. The supreme properties of porous structures arise from their complex geometries and topologies, particularly the structural heterogeneity and anisotropy, which have been tailored through thousand-year evolution given the competing constraints in nature [5]. These porous structures usually have fully interconnected pore networks within their interiors so as to enhance nutrition transfer or attachment, or to provide sufficient space for regeneration in tissue engineering [6]. The interconnection property is also mandatory when fabricating such porous structures by means of additive manufacturing, so that the unnecessary support structures during fabrication can be cleaned during postprocessing [7]. However, approaches for the efficient design of such interconnected heterogeneous porous structures have seldom been presented.

We study the problem of designing a heterogeneous interconnected porous structure while simultaneously maintaining a high degree of mechanical and structural rigidity. The macro-design mesh is assumed fixed in the study so that we

* Corresponding authors.
E-mail addresses: li.jz@sustech.edu.cn (J. Li), kzhang@jlu.edu.cn (K. Zhang).

https://doi.org/10.1016/j.jcp.2020.109909
0021-9991/

have restricted the design space and thereby formulated a well-posed design optimization problem. The challenges of this problem lie in its proper geometric modeling, efficient performance simulation, and reliable design optimization.

In terms of the geometric modeling aspect, most conventional methods have mainly assumed a homogeneous element distribution, which only allows for rough shape tuning using parameters relating to the porosity and pore size. However, to utilize the design potentiality of porous structures maximally, it is highly necessary to model and control both the directional anisotropy and distributional heterogeneity. To achieve this goal, the concept of the *extended triply periodic minimal surface* (ETPMS) is introduced, whereby the structural volume is prescribed using an *implicitly defined surface* under shape control parameters. In contrast to its counterpart the triply periodic minimal surface (TPMS), the ETPMS exhibits additional design freedom along three axis directions, further enhancing the element anisotropy. Moreover, instead of using discrete constant design variables in each cell, the ETPMS controls the element distribution using certain continuous controlling parameter fields, thereby enabling smooth transition between adjacent elements. Consequently, the consistent implicit definition of the ETPMS is expected to offer significant advantages in terms of continuous connectivity, structural integrity, and the distinctive properties of porous structures; compared to conventional lattice- or strut-based architectures, the ETPMS does not have joints and struts along the body.

The modeling advantages of the ETPMS come at the cost of challenges in terms of its efficient simulation. Conventional approaches [8–14] generally simulated the performance of such biscale structures via numerical homogenization, which computes an effective elasticity tensor for each microstructure via finite element (FE) analysis and substantially reduces the overall simulation costs. However, the costs remain high as the homogenization process must be conducted for each microstructure during each optimization iteration. We resolve the issue using the strategy of offline pre-computed parametric homogenization, which explicitly expresses the material property as a function of the ETPMS design parameters and can thus instantly simulate the property of an ETPMS element at any specific parameter. It ultimately not only avoids the complex remeshing process, but also facilitates the process by building on a previous study on *proper generalized decomposition* (PGD) [15].

A further disadvantage lies in the effective and efficient optimization owing to the implicitly defined shape description. A set of validity constraints must be prescribed for each ETPMS element for the ETPMS-based porous structure to be solid and/or core connected. This induces a significant number of constraints for the design optimization problem and makes it difficult to derive a converged solution efficiently. The numerical techniques of constraint aggregation and adjoint-based sensitivity computation are introduced to resolve the issue. Ultimately, the proposed approach can produce smooth and heterogeneous porous structures with scaled anisotropy and fully interconnected pore networks for performance optimization, as demonstrated via a suite of three-dimensional (3D) benchmark examples.

The main contributions of this study are as follows: An approach is proposed using *implicit* surfaces to design heterogeneous and anisotropic porous structures with fully interconnected pore networks, as well as a systematic approach for the implementation. The concept of ETPMS is presented for modeling the interconnected heterogeneous porous structures with consistent anisotropy and heterogeneity control, and a sufficient condition on its geometric validity is provided. Offline parametric homogenization is conducted based on PGD to predict the properties of a range of microstructures with high accuracy. A specially tailored biscale optimization approach for the ETPMS, in combination with the techniques of offline pre-computation and sensitivity computation, is demonstrated via various 3D numerical examples.

The remainder of this paper is organized as follows: pertinent studies are briefly reviewed in Section 2. The concept of the ETPMS is proposed, and its analytical and geometrical properties are described in Section 3. Thereafter, the problem of designing a heterogeneous porous structure for physical performance optimization is formulated in Section 4. The approach for computing the parametric homogenized material properties using PGD is presented in Section 5. The overall numerical optimization approach is outlined in Section 6. The numerical results from benchmark examples are discussed in Section 7. Finally, we conclude the paper in Section 8.

2. Review of pertinent studies

The current study is closely related to porous structure modeling, the TPMS, biscale topology optimization, and model reduction. Existing work on these topics is briefly reviewed in this section.

2.1. Porous structure modeling and TPMS

Heterogeneous and anisotropic porous structures exist ubiquitously in nature and have attracted substantial attention from researchers in the past several decades, particularly in the fields of bone tissue engineering [16] and material science [17]. The majority of these studies focused on the fabrication of porous structures using chemical or physical approaches, but provided little capability to control the modeling geometries. In recent years, the precise modeling of heterogeneous and anisotropic porous structures has started to attract more research interest with the development of additive manufacturing technologies, which significantly facilitate the precise fabrication of any geometrically complex structures. For example, Kou and Tan [18] initiated an approach to design irregular porous artifacts with controllable pore shapes and distributions based on Voronoi tessellations. Furthermore, Gómez et al. [19] used the Voronoi tessellation to design bone-like porous scaffolds.

TPMS elements have been applied for modeling porous structures in previous studies. For example, a generalized periodic surface model was used in [20] to reconstruct the loci surfaces of crystals. Traditional TPMS elements are always periodically distributed in space, and in this study, they are extended to model porous structures so that the distribution and anisotropy of each element can be controlled precisely and explicitly with additional degrees of freedom. The modeling of heterogeneous porous structures for a smooth transition between adjacent TPMS elements with different shape parameters was also studied by Yoo [21]. In this study, the approach is extended to generate a smooth ETPMS with enhanced anisotropy control, and the overall distributions are further optimized to improve the elastic performance of the generated porous structure.

2.2. Biscale topology optimization

In this study, the performance of the porous structures is optimized within a biscale optimization framework, which is closely related to studies on topology optimization. In one of the pioneering works in topology optimization, Bendsøe and Kikuchi first proposed a homogenization-based topology optimization approach [8], in which the hole size parameters and an orientation parameter within each design element were iteratively optimized to produce an optimized structure. As opposed to our study, which focuses on porous structure design, the approach in [8] aimed to produce an optimized structure on the macroscale. Thus, it did not involve issues such as the porous structure modeling and its geometric validity, or forming an interconnected pore network within their interiors.

Biscale topology optimization has recently attracted extensive research interest, whereby both the macrostructure and microstructure densities have been taken as design variables and iteratively updated to optimal values [8–14]. Although biscale topology optimization has been demonstrated in creating complex structures with supreme properties, it still faces challenges, particularly expensive simulation costs and disconnection between adjacent elements. To reduce the computational costs, solutions based on meta-modeling or surrogate models have been proposed [22,23]. In our study, a PGD-based acceleration process is proposed to resolve this issue by constructing direct mapping from the design parameters to their associated effective elasticity tensors.

The geometric disconnection between adjacent micro-elements arises from the assumption of scale separation in homogenization-based simulation, which is involved in biscale optimization approaches. Consequently, the optimized overall structure does not necessarily form an integral part and is usually inferior to the designed structure [24]. This critical issue has recently attracted significant research interest, and several approaches based on geometric or physical constraints have been proposed [25,24,13,14]. In particular, Zong et al. proposed a variable cutting (VCUT) level set that uses a continuous cutting function by interpolating a set of height variables to generate functionally graded cellular structures, and ultimately achieved perfect geometric connections between adjacent cells [13]. This concept is similar to our proposal for creating a heterogeneous smooth ETPMS using interpolation functions on the controlling parameters.

Moreover, specific material anisotropy has been explored for structure optimization. For example, Liu and Shapiro [26] realigned the orientations of microstructures inside macrostructures according to the material orientation obtained from topology optimization. Compared to the extensive studies on general biscale topology optimization, the design of an optimal structure made of specific anisotropic materials has undergone relatively little investigation. In recent years, Regazzoni et al. [27] constructed optimal multimaterial structures of minimum compliance using self-assembling diblock copolymers, the effective elastic properties of which were controlled by a scalar parameter and orientations of the anisotropy.

2.3. PGD

In this study, a model reduction approach, namely PGD, is applied to reduce the computational costs. PGD [15] is a novel model reduction approach that was recently developed for efficiently calculating a parametric simulation solution. The approach has been studied for various physical problems, such as viscous fluid motion simulation [28], heat problems [29], and linear elasticity [30]. We extend it to compute the parametric effective material properties for microstructures under parametric variations. In contrast to previous PGD studies, which have generally been conducted in a fixed computational domain, the computational domains studied in this work are not only varied by control parameters, but are also defined by implicit functions. This difference results in further issues in the efficient integral computation involved in computing each element of the associated stiffness matrix and elasticity tensor.

3. Extended triply periodic minimal surface (ETPMS)

We first introduce the following notations used throughout the paper. Let $\Omega := \{\Omega_e\}^N \subset \mathbb{R}^3$ be a fixed 3D macro-design domain consisting of cubic elements Ω_e, $e = 1, \ldots, N$, and Γ_D and Γ_N are the fixed boundary and loading boundary, respectively. Let $\mathbf{x} := (x, y, z) \in \Omega$ be the spatial Cartesian coordinate of a point in Ω, and $\mathbf{s} := \{\mathbf{s}_e = (a_e, b_e, c_e) \in I,\ e = 1, \ldots, N\}$ is the vector of control parameters defined on each cell Ω_e; I is the range of the parameters so that a connected ETPMS is generated. Accordingly, a set of discrete ETPMS elements $\phi(\mathbf{x}, \mathbf{s}) := \{\phi(\mathbf{x}, \mathbf{s}_e)\}^N$ is defined, where each element $\phi(\mathbf{x}, \mathbf{s}_e)$ is described by the control parameter $\mathbf{s}_e$ for an implicitly defined function. We also rewrite $\phi(\mathbf{x}, \mathbf{s}), \phi(\mathbf{x}, \mathbf{s}_e)$ as $\phi(\mathbf{s}), \phi(\mathbf{s}_e)$ for simplicity. We denote $\phi_c(\mathbf{s}(\mathbf{x}))$ as the continuous ETPMS (or c-ETPMS) to model a porous structure under a parametric control function vector $\mathbf{s}(\mathbf{x})$ over the domain Ω. We present the details thereof in Section 3.2.

Table 1
Functions of typical TPMS.

Type	Function
P	$\cos X + \cos Y + \cos Z - c = 0$
D	$\cos X \cos Y \cos Z - \sin X \sin Y \sin Z - c = 0$
G	$\sin X \cos Y + \sin Z \cos X + \sin Y \cos Z - c = 0$
$I\text{-}WP$	$2(\cos X \cos Y + \cos Y \cos Z + \cos Z \cos X) - (\cos 2X + \cos 2Y + \cos 2Z) - c = 0$
$F\text{-}RD$	$-(\cos 2X \cos 2Y + \cos 2X \cos 2Z + \cos 2Y \cos 2Z) + 4 \cos X \cos Y \cos Z - c = 0$

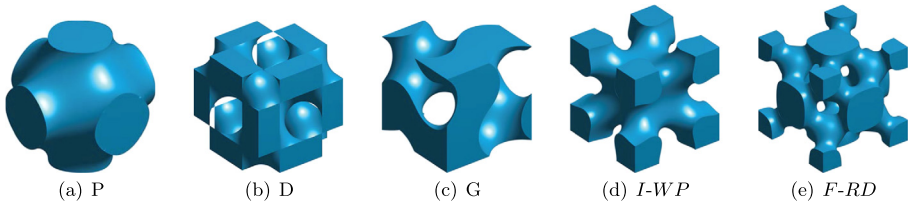

Fig. 1. Shapes of typical TPMS elements.

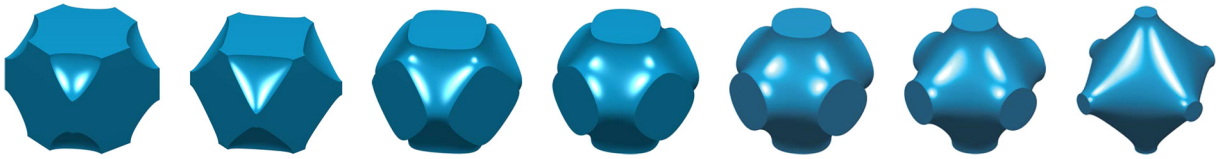

Fig. 2. P elements with parameter c changing from left to right, from -1.5 to 0.9 in a step of 0.4.

We formulate the problem of the heterogeneous porous structure design as determining the optimal distribution of $\phi(\mathbf{s}) = \{\phi(\mathbf{s}_e)\}^N$ under certain controlling parameters $\mathbf{s}$ for overall physical performance optimization. The postprocessing yields a smooth porous structure defined by a c-ETPMS $\phi_c(\mathbf{s}(\mathbf{x}))$.

In the following, we first recall the classical TPMS, and then propose the concept of the ETPMS and c-ETPMS. A sufficient condition on the geometric connection of an ETPMS is also derived.

3.1. Triply periodic minimal surface (TPMS)

TPMS shapes have been found in copolymers, crystals, biological membranes, and many other areas of natural science, and have received attention from structural physicists and material scientists. They are minimal surfaces in $\mathbb{R}^3$, with a zero mean curvature and periodicity in three independent directions. We refer to the volume enclosed by a TPMS in one periodicity as a *TPMS element*.

The classical TPMS includes the P, D, G, $I\text{-}WP$, and $F\text{-}RD$ types, and these are usually defined via implicit functions $\phi(c) = 0$, as listed in Table 1 and depicted in Fig. 1. We use the P type as an example without loss of generality. A TPMS $\phi(c) = 0$ separates the unit cell Ω_e into two parts: the solid part defined by $\phi(c) \geq 0$ and the void or pore part defined by $\phi(c) < 0$. In particular, a P-type element over a cubic unit cell $\Omega_e = [x_0, x_0 + 1] \times [y_0, y_0 + 1] \times [z_0, z_0 + 1]$, $x_0, y_0, z_0 \in \mathbb{Z}$ is defined as follows:

$$\phi(c) = \cos(2\pi x - \pi) + \cos(2\pi y - \pi) + \cos(2\pi z - \pi) - c \geq 0, \ [x, y, z] \in \Omega_e, \tag{1}$$

where c is a constant controlling the element shape.

As can be observed from Fig. 2, a smaller value of c results in a larger solid volume of the associated element $\phi(c)$.

3.2. Extended TPMS of controlled anisotropy

The concept of the ETPMS is introduced, which has a different anisotropy control parameter along a different axis direction.

Definition 1 *(ETPMS).* An ETPMS element of type P inside a cubic unit cell Ω_e is defined as follows:

$$\phi(r, s, t, p) = r \cos(2\pi x - \pi) + s \cos(2\pi y - \pi) + t \cos(2\pi z - \pi) - p \geq 0, \ [x, y, z] \in \Omega_e, \tag{2}$$

where $r, s, t \neq 0$, p are constant parameters controlling the ETPMS element shape.

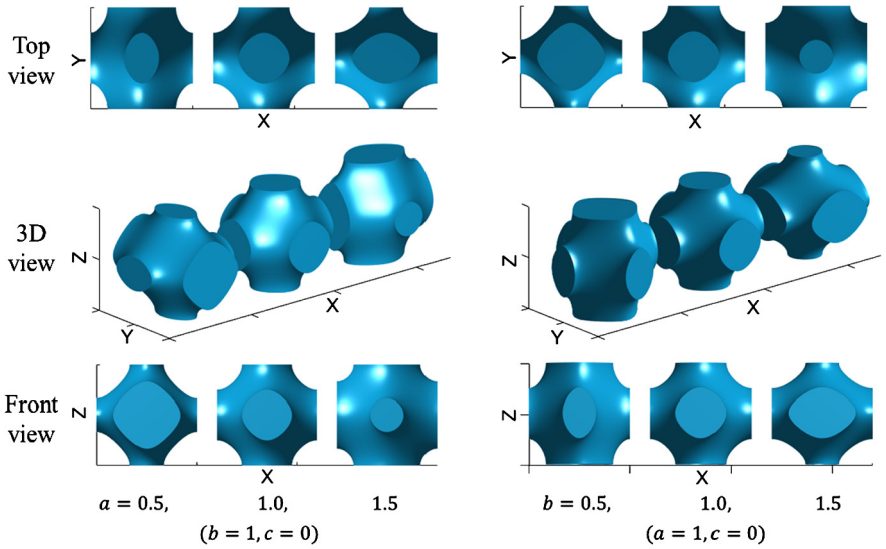

Fig. 3. Extended P surface elements when $c = 0$ and a, b take different values. Each cell can be extended periodically in space along the x, y, and z directions.

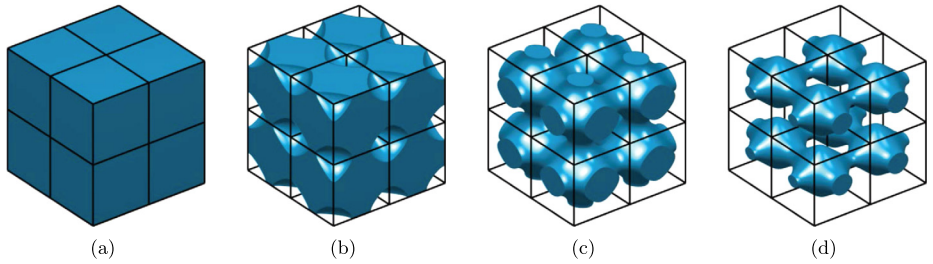

Fig. 4. $2 \times 2 \times 2$ tiling of extended P elements with different c values, representing connected or unconnected solids or pores: (a) fully filled; (b) pores not connected; (c) well-connected solids and pores; and (d) solids not connected.

As $r \neq 0$, we rewrite (2) as follows for simplicity:

$$\phi(a, b, c) = \cos(2\pi x - \pi) + a\cos(2\pi y - \pi) + b\cos(2\pi z - \pi) - c \geq 0, \tag{3}$$

where $a = s/r$, $b = t/r$, and $c = p/r$. We also denote $\mathbf{s}_e = (a, b, c)$ for simplicity. In Fig. 3, the shapes for different a, b, and c are plotted.

3.3. Range of parameters for volume connection

An ETPMS element $\phi(\mathbf{s}_e)$ within a cubic unit cell Ω_e divides the space into two volumetric structures $\phi(\mathbf{s}_e)$ and $\Omega_e \setminus \phi(\mathbf{s}_e)$, known as the solid and pore, respectively. We aim to construct a connected ETPMS in both parts. However, different values of $\mathbf{s}_e = (a, b, c)$ in (3) may produce well-connected or disconnected solids or pores (see, for example, Fig. 4). The range with respect to the parameters a, b, c must be properly determined for structural validity, as explained in the following.

The range of the parameters (a, b, c) is determined by taking into account the three types of colored points in Fig. 5: red, blue, and green, respectively. The relative locations of these points with respect to the ETPMS indicate the connections of the solid or pore parts, based on which we can specify the associated parameter range.

First, consider the extreme case in which the solid element fully fills the cubic unit cell. The condition is satisfied if the eight red points in Fig. 5 all lie within the volume element; that is, $\phi(\mathbf{x}, \mathbf{s}_e) \leq 0$ for the points $\mathbf{x} = (l_1, l_2, l_3)$, $l_1, l_2, l_3 \in \{0, 1\}$, which yields:

$$1 + a + b + c \geq 0 \Longrightarrow \text{An ETPMS element is within the unit cubic cell.} \tag{4}$$

Next, the solid part of an ETPMS element is connected if the central green points on the six faces of the cubic unit cell in Fig. 5 all lie within the ETPMS element; that is, $\phi(\mathbf{x}, \mathbf{s}_e) \geq 0$ for $\mathbf{x} = (l_1, 0.5, 0.5)$, $(0.5, l_1, 0.5)$, $(0.5, 0.5, l_1)$, $l_1 \in \{0, 1\}$, which yields:

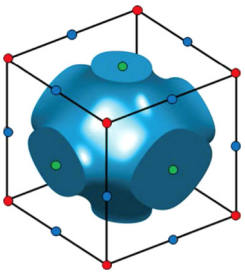

Fig. 5. Description of sufficient condition on solid and pore connections of ETPMS element. (For interpretation of the colors in the figure(s), the reader is referred to the web version of this article.)

$$\begin{cases} -1+a+b-c \geq 0 \\ 1-a+b-c \geq 0 \\ 1+a-b-c \geq 0 \end{cases} \Longrightarrow \text{a solid-connected ETPMS element.} \tag{5}$$

Similarly, the interior porous network (determined as $\Omega \setminus \phi(\mathbf{x}, \mathbf{s}_e)$) is fully connected if the blue midpoints of the 12 edges in Fig. 5 are not within the solid ETPMS element; that is, $\phi(\mathbf{x}, \mathbf{s}_e) < 0$ for $\mathbf{x} = (0.5, l_1, l_2)$, $(l_1, 0.5, l_2)$, $(l_1, l_2, 0.5)$, $l_1, l_2 \in \{0, 1\}$, which yields:

$$\begin{cases} 1-a-b-c < 0 \\ -1+a-b-c < 0 \\ -1-a+b-c < 0 \end{cases} \Longrightarrow \text{a pore-connected ETPMS element.} \tag{6}$$

Summarizing the above results, we obtain the following important lemma.

Lemma 1. *Given an ETPMS described by (3), the following properties are verified:*

- *The solid part is connected if both (4) and (5) are satisfied, the range of which is denoted by I^s. The condition is specified as $\mathbf{s}_e \in I^s$.*
- *Both the solid and porous regions are connected if (4), (5), and (6) are all satisfied, the range of which is denoted by I^{sp}. The condition is specified as $\mathbf{s}_e \in I^s$.*

The two types of parameter ranges prescribed by Lemma 1 are illustrated in Fig. 6 as I^s and I^{sp}, respectively. Note that the range I^s is a cone-like polyhedron and the range I^{sp} is a subset of I^s, where the values of the parameters a, b, c in I^s or I^{sp} may approach infinity; see also Fig. 6(b). Moreover, we note in Fig. 6(a) that different values of $\mathbf{s}_e$ produce very different types of ETPMS elements, which exhibit different material properties.

3.4. c-ETPMS

The ETPMS described above has a constant value $\mathbf{s}_e = \{(a, b, c)\}$ in each cell, and the adjacent elements are not smoothly connected for different values of $\mathbf{s}_e$ within different cubic cells. To produce smooth, heterogeneous porous structures with controllable anisotropy, we further introduce the concept of the c-ETPMS, which replaces the constant parameters a, b, c in (3) with the continuous functions $a(\mathbf{x}), b(\mathbf{x}), c(\mathbf{x})$. The continuity of the control parameters ensures a smooth transition between adjacent ETPMS cells.

Definition 2 *(c-ETPMS).* A c-ETPMS element under control parameter $\mathbf{s}$ is defined as follows:

$$\phi_c(\mathbf{s}) = \cos(2\pi x - \pi) + a(\mathbf{x})\cos(2\pi y - \pi) + b(\mathbf{x})\cos(2\pi z - \pi) - c(\mathbf{x}) \geq 0. \tag{7}$$

An example of a c-ETPMS is presented in Fig. 7. Note that the continuous functions $a(\mathbf{x}), b(\mathbf{x}), c(\mathbf{x})$ can be defined by various types of interpolation functions, as discussed further in Section 6.4.

4. Problem statement and approach overview

We aim to optimize an interconnected porous structure using the c-ETPMS for performance optimization. The problem is first described within the context of the well-studied compliance minimization problem of linear elasticity analysis, which is followed by an overview of the approach.

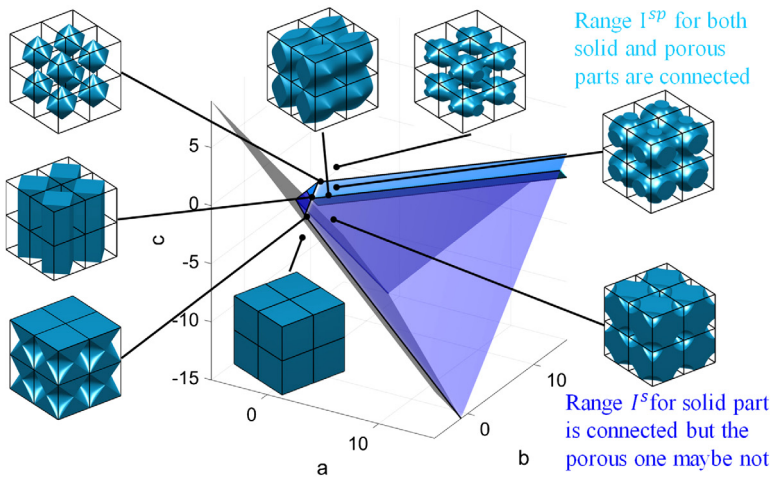

(a) Parameter range I^s produces ETPMS elements that are solid connected but pores not connected (dark blue), while parameter range I^{sp} produces ETPMS elements that are both solid and pores connected (light blue)

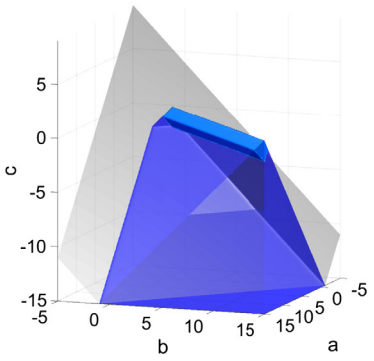

(b) Different viewpoint of (a)

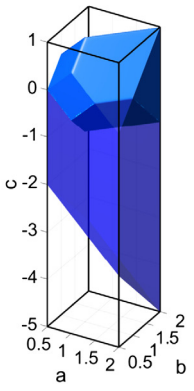

(c) The intersections between I^s, I^{sp} with a local range L.

Fig. 6. Different ranges of parameters a, b, c in (3) determine different solid or pore connections of ETPMS elements. $L = [0.5, 2] \times [0.5, 2] \times [-5, 1]$.

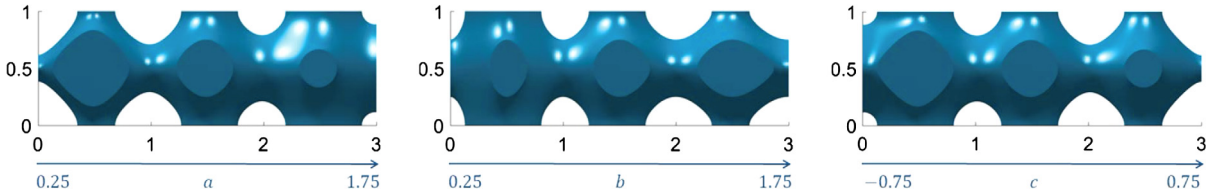

(a) a varies (b) b varies (c) c varies

Fig. 7. c-ETPMS defined by continuous parameter functions: (a) $a(x, y, z) = 0.5x + 0.25$, $b(x, y, z) = 1$, $c(x, y, z) = 0$; (b) $b(x, y, z) = 0.5x + 0.25$, $a(x, y, z) = 1$, $c(x, y, z) = 0$; and (c) $c(x, y, z) = 0.5x - 0.75$, $a(x, y, z) = 1$, $b(x, y, z) = 1$.

4.1. Problem statement

Given a fixed discrete macro-design mesh $\{\Omega_e\}^N$ for a design domain Ω under external loading, as illustrated in Fig. 8, we aim to determine an interconnected heterogeneous porous structure defined by a c-ETPMS; that is, $\phi_c(a(\mathbf{x}), b(\mathbf{x}), c(\mathbf{x}))$ in (7) or $\phi_c(\mathbf{s}(\mathbf{x}))$ for short, for its compliance minimization. Note the macro-design mesh is assumed fixed in the study so that we have restricted the design space and thereby formulated a well-posed design optimization problem.

This problem is formulated as follows: Find the c-ETPMS $\phi_c(\mathbf{s}(\mathbf{x}))$

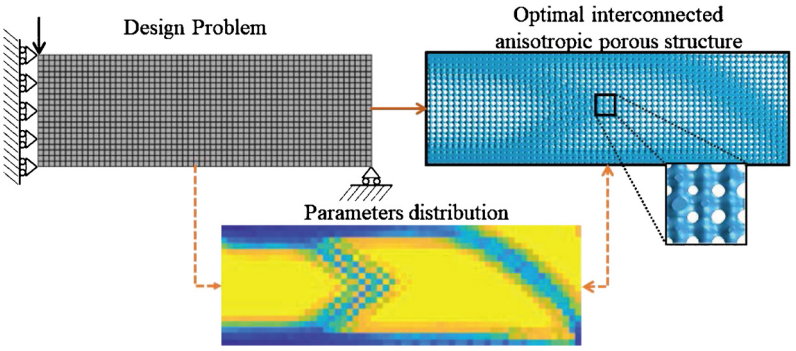

Fig. 8. Problem of optimal interconnected anisotropic porous structure design.

$$(\textbf{Problem}: P_O) \qquad \min_{\mathbf{s}(\mathbf{x})} C(\mathbf{u}, \mathbf{s}(\mathbf{x})), \text{ compliance minimization,}$$

$$\text{s.t.} \quad \begin{cases} \alpha(\mathbf{u}, \mathbf{v}) = l(\mathbf{v}), \mathbf{v} \in U_0, & \text{equilibrium equation,} \\ \frac{V(\phi_c(\mathbf{s}(\mathbf{x})))}{|\Omega|} \leq \mathcal{V}, & \text{volume fraction constraint.} \end{cases} \tag{8}$$

In the above, $\mathbf{s}(\mathbf{x}) = (a(\mathbf{x}), b(\mathbf{x}), c(\mathbf{x}))$ is the design function to be optimized, U_0 prescribes an appropriate admissible space, and

$$C(\mathbf{u}, \mathbf{s}(\mathbf{x})) = \int_{\phi_c(\mathbf{s}(\mathbf{x}))} \boldsymbol{\epsilon}(\mathbf{u}) : \mathbf{D} : \boldsymbol{\epsilon}(\mathbf{u})\, dV, \tag{9}$$

$$\alpha(\mathbf{u}, \mathbf{v}) = \int_{\phi_c(\mathbf{s}(\mathbf{x}))} \boldsymbol{\epsilon}(\mathbf{u}) : \mathbf{D} : \boldsymbol{\epsilon}(\mathbf{v})\, dV, \quad l(\mathbf{v}) = \int_{\Gamma_N} \boldsymbol{\tau} \cdot \mathbf{v}\, d\Gamma, \tag{10}$$

where $\boldsymbol{\tau}$ is the external loading on boundary Γ_N, $\boldsymbol{\epsilon}$ is the strain in terms of the displacement field $\mathbf{u}$, $\mathbf{D}$ is the elasticity tensor, and $V(\phi_c(\mathbf{s}(\mathbf{x})))$ is the volume of $\phi_c(\mathbf{s}(\mathbf{x}))$.

It is very challenging to resolve the above optimization problem directly, and we thus approximate the c-ETPMS, $\phi_c(\mathbf{s}(\mathbf{x}))$, using a set of discrete ETPMSs $\{\phi(\mathbf{s}_e)\}$, in which each ETPMS $\phi(\mathbf{s}_e)$ has a constant value of parameter $\mathbf{s}_e$ within a cubic cell Ω_e. Furthermore, we apply numerical homogenization techniques to approximate the material property of each ETPMS element $\phi(\mathbf{s}_e)$ to improve the computational efficiency, as also widely conducted in traditional concurrent topology optimization approaches [8–12,14]. The consideration consequently leads to the following new problem formulation:

Find the discrete design variables $\mathbf{s} = \{\mathbf{s}_e\} \in \mathbb{R}^{N\times 3}$ satisfying

$$(\textbf{Problem}: P_H) \qquad \min_{\mathbf{s}=\{\mathbf{s}_e\}\in\mathbb{R}^{N\times 3}} C(\mathbf{u}, \mathbf{s}), \text{ compliance minimization,}$$

$$\text{s.t.} \quad \begin{cases} \alpha(\mathbf{u}, \mathbf{v}) = l(\mathbf{v}), \mathbf{v} \in U_0, & \text{equilibrium equation,} \\ \frac{V(\phi(\mathbf{s}))}{|\Omega|} \leq \mathcal{V}, & \text{volume fraction constraint,} \end{cases} \tag{11}$$

where $\phi(\mathbf{s}) = \{\phi(\mathbf{s}_e)\}$, and

$$C(\mathbf{u}, \mathbf{s}) = \int_{\phi(\mathbf{s})} \boldsymbol{\epsilon}(\mathbf{u}) : \mathbf{D}^H : \boldsymbol{\epsilon}(\mathbf{u})\, dV = \sum_e \int_{\phi(\mathbf{s}_e)} \boldsymbol{\epsilon}(\mathbf{u}) : \mathbf{D}_e^H : \boldsymbol{\epsilon}(\mathbf{u})\, dV, \tag{12}$$

$$\alpha(\mathbf{u}, \mathbf{v}) = \int_{\phi(\mathbf{s})} \boldsymbol{\epsilon}(\mathbf{u}) : \mathbf{D}^H : \boldsymbol{\epsilon}(\mathbf{v})\, dV = \sum_e \int_{\phi(\mathbf{s}_e)} \boldsymbol{\epsilon}(\mathbf{u}) : \mathbf{D}_e^H : \boldsymbol{\epsilon}(\mathbf{v})\, dV, \quad l(\mathbf{v}) = \int_{\Gamma_N} \boldsymbol{\tau} \cdot \mathbf{v}\, d\Gamma, \tag{13}$$

$$V(\phi(\mathbf{s})) = \sum_e V(\phi(\mathbf{s}_e)) \tag{14}$$

is the volume enclosed by $\phi(\mathbf{s})$, and $\mathbf{D}_e^H$ is the homogenized elasticity tensor for each ETPMS element $\phi(\mathbf{s}_e)$.

The effective elasticity tensor $\mathbf{D}_e^H$ for an ETPMS element $\phi(\mathbf{s}_e)$ has conventionally been evaluated using a numerical homogenization technique. As the homogenization process must be performed for each microstructure $\phi(\mathbf{s}_e)$ during each iterative optimization process, it remains very computationally expensive. We address this issue by further expressing $\mathbf{D}_e^H$ as an explicit function of the design parameters $\mathbf{s}_e$; that is, $\mathbf{D}_e^H(\mathbf{s}_e)$, the derivation of which is detailed in Section 5.

This results in the following optimization problem: find the design variables $\mathbf{s} = \{\mathbf{s}_e\} \in \mathbb{R}^{N\times 3}$ satisfying

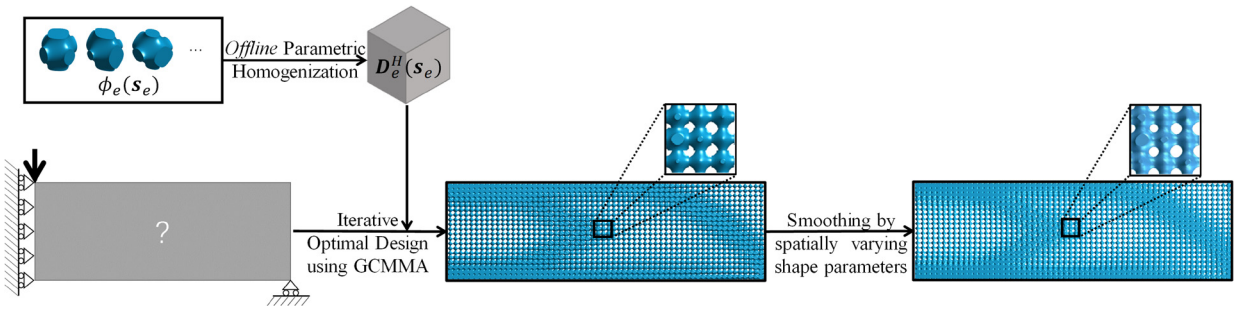

Fig. 9. Flowchart for designing optimization of heterogeneous interconnected porous structures using ETPMS.

$$(\textbf{Problem}: P_D) \qquad \min_{\mathbf{s}=\{\mathbf{s}_e\}\in\mathbb{R}^{N\times 3}} C(\mathbf{u},\mathbf{s}), \text{ compliance minimization,}$$

$$\text{s.t.} \quad \begin{cases} \mathbf{K}(\mathbf{s})\mathbf{u}=\mathbf{f},\ \mathbf{u}\in\mathbb{R}^n, & \text{equilibrium equation,} \\ \frac{V(\mathbf{s})}{|\Omega|}\le\mathcal{V}, & \text{volume fraction constraint,} \\ \mathbf{s}_e\in I_{\mathbf{s}}, & \text{interconnection constraint,} \end{cases} \tag{15}$$

where $I_{\mathbf{s}}=I^s$ or I^{sp} is the parameter range defined in Lemma 1, prescribing the conditions on the solid or pore interconnection, $\mathbf{u}\in\mathbb{R}^n$ is the vector of nodal displacements to be computed, $\mathbf{f}$ represents the vector of external loading, and $\mathbf{K}(\mathbf{s})$ is the overall stiffness matrix assembled cell by cell,

$$\mathbf{K}(\mathbf{s})=\sum_{e=1}^{N}\mathbf{K}(\mathbf{s}_e)=\sum_{e=1}^{N}\int_{\Omega_e}\mathbf{B}^T\mathbf{D}_e^H(\mathbf{s}_e)\mathbf{B}\,dV, \tag{16}$$

for the strain–displacement matrix $\mathbf{B}$, the target compliance

$$C(\mathbf{u},\mathbf{s})=\mathbf{u}^T\mathbf{K}(\mathbf{s})\mathbf{u}=\sum_{e}\mathbf{u}_e^T\mathbf{K}(\mathbf{s}_e)\mathbf{u}_e, \tag{17}$$

and $V(\mathbf{s})=\sum_e V(\mathbf{s}_e)$ is the sum of the volume enclosed by an ETPMS element $\phi(\mathbf{s}_e)$.

4.2. Approach overview

As illustrated in Fig. 9, the overall approach for the design optimization of heterogeneous interconnected porous structures using ETPMS consists of three main steps. First, offline parametric homogenization is conducted, building on previous studies of PGD, which ultimately expresses the effective elasticity tensor $\mathbf{D}^H(\mathbf{s}_e)$ for an ETPMS cell as an explicit function with respect to the design parameter $\mathbf{s}_e$.

Next, a biscale design optimization is performed to derive the optimal discrete ETPMS parameters $\{\mathbf{s}_e,\ \Omega_e\in\Omega\}$. Compared to previous biscale parameter/topology optimization approaches, the studied optimization problem exhibits at least two challenges. First, the computational domains are varied during the optimization process, as described by an implicit function under different control parameters instead of the fixed computational domain that has popularly been studied previously. A remeshing process for elasticity analysis would thus be costly, and we deal with this issue by introducing a characteristic function so that a fixed computational domain is used during the optimization iterations. Second, a nontrivial range of design variables is prescribed for each cell Ω_e so that a valid ETPMS cell can always be generated, as indicated in Lemma 1. This results in a large number of nontrivial optimization constraints and adds substantial difficulty in computing an optimized solution. In contrast, previous studies on design optimization have simply involved a single variable per element, or have used multiple variables under trivial lower and upper bounds on each one [14]. The numerical techniques of constraint aggregation and adjoint-based sensitivity computation are introduced to resolve the issue.

Finally, once the discrete shape vector $\mathbf{s}=\{\mathbf{s}_e\}$ is obtained, a perfectly smooth porous structure is constructed by interpolating the discrete shape parameters $\{\mathbf{s}_e\}$, consequently yielding the target c-ETPMS $\phi_c(\mathbf{s}(\mathbf{x}))$.

The details underlying the approach are explained further below.

5. Computing parametric homogenized material properties using PGD

The homogenized property $\mathbf{D}_e^H$ of a microstructure $\phi(\mathbf{s}_e)$ inside a cell Ω_e is determined by its configuration; specifically, the shape parameter $\mathbf{s}_e$. We construct the property $\mathbf{D}^H(\mathbf{s}_e)$ explicitly in terms of $\mathbf{s}_e$ by building on previous work on PGD [15].

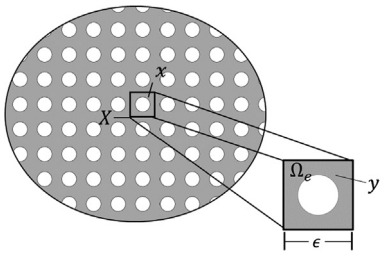

Fig. 10. Macro- and microscale in the homogenization theory.

5.1. Problem of parametric homogenization

Numerical homogenization provides a two-step approach for calculating the effective material property corresponding to a representative volume element (RVE), assuming that the RVE size is relatively sufficiently small as a homogenized point on the macroscopic scale. Consider the porous structure Ω in Fig. 10. Let Ω_e be the X-th cell with respect to Ω, or the cell coordinate on the macroscale, and ϵ be the cell size. Let $\mathbf{y}$ be the coordinate of a point inside Ω_e on the microscale, and $\mathbf{x}$ the coordinate of the point in the macroscale. Correspondingly, we obtain the association between the micro- and macro-coordinates:

$$\mathbf{x} = \mathbf{X} + \mathbf{y}, \quad 0 \le \mathbf{y} \le \epsilon. \tag{18}$$

For the linear elasticity problem under investigation, the homogenization theory aims to approximate the elasticity tensor $\mathbf{D}^H(\Omega_e)$ for each cell Ω_e by equalizing their strain energy at the macro- and micro-scales, as stated below.

Lemma 2. *[31,8,32] Let $\mathbf{D}_{ijpq}(\Omega_e, \mathbf{y})$ be the elasticity tensor at every micro-point $\mathbf{y}$ for a microstructure $\phi(\mathbf{s}_e)$ within a cell Ω_e. For each specific pair of $1 \le i, j, k, l \le 3$, each component of the homogenized elasticity tensor $\mathbf{D}^H_{ijkl}(\phi(\mathbf{s}_e))$ can be approximated as*

$$\mathbf{D}^H_{ijkl}(\phi(\mathbf{s}_e)) = \frac{1}{|\phi(\mathbf{s}_e)|} \int_{\phi(\mathbf{s}_e)} (\mathbf{D}_{ijkl}(\phi(\mathbf{s}_e), \mathbf{y}) - \mathbf{D}_{ijpq}(\phi(\mathbf{s}_e), \mathbf{y}) \frac{\partial \boldsymbol{\mu}^{kl}_p}{\partial \mathbf{y}_q}) d\mathbf{y}, \tag{19}$$

where the summation convention is used here and henceforth, and each periodic unit strain displacement $\boldsymbol{\mu}^{kl}$ is obtained by satisfying

$$\int_{\phi(\mathbf{s}_e)} (\mathbf{D}_{ijkl}(\phi(\mathbf{s}_e), \mathbf{y}) - \mathbf{D}_{ijpq}(\phi(\mathbf{s}_e), \mathbf{y}) \frac{\partial \boldsymbol{\mu}^{kl}_p}{\partial \mathbf{y}_q}) \frac{\partial \mathbf{v}_i}{\partial \mathbf{y}_j} d\mathbf{y} = 0, \tag{20}$$

for all periodic $\mathbf{v}$.

Equation (20) can be rewritten in the following form

$$A(\boldsymbol{\mu}^{kl}, \mathbf{v}) = L(\mathbf{v}), \tag{21}$$

for all kinematically admissible $\mathbf{v}$, where

$$A(\boldsymbol{\mu}^{kl}, \mathbf{v}) = \int_{\Omega_e} \mathbf{D}_{ijpq}(\Omega_e, \mathbf{y}) \frac{\partial \boldsymbol{\mu}^{kl}_p}{\partial \mathbf{y}_q} \frac{\partial \mathbf{v}_i}{\partial \mathbf{y}_j} \, d\mathbf{y}, \quad L(\mathbf{v}) = \int_{\Omega_e} \mathbf{D}_{ijkl}(\Omega_e, \mathbf{y}) \frac{\partial \mathbf{v}_i}{\partial \mathbf{y}_j} \, d\mathbf{y}, \tag{22}$$

with periodic boundary conditions.

The aim of the parametric homogenization is to compute the displacement $\boldsymbol{\mu}^{kl}(\mathbf{y})$ in (21) as a function of the space coordinate $\mathbf{y}$ and ETPMS control parameter $\mathbf{s}_e$, denoted by $\boldsymbol{\mu}^{kl}(\mathbf{y}, \mathbf{s}_e)$. Accordingly, the numerical homogenization problem (21) is transformed into a parametric form: find solution $\boldsymbol{\mu}^{kl}(\mathbf{y}, \mathbf{s}_e)$ such that

$$A_{\mathbf{s}_e}(\boldsymbol{\mu}^{kl}, \mathbf{v}) = L_{\mathbf{s}_e}(\mathbf{v}), \tag{23}$$

where

$$A_{\mathbf{s}_e}(\boldsymbol{\mu}^{kl}, \mathbf{v}) = \int_{I_{\mathbf{s}}} \int_{\phi(\mathbf{s}_e)} \bar{\mathbf{D}}_{ijpq} \frac{\partial \boldsymbol{\mu}^{kl}_p}{\partial \mathbf{y}_q} \frac{\partial \mathbf{v}_i}{\partial \mathbf{y}_j} \, d\mathbf{y} d\mathbf{s}_e, \quad L_{\mathbf{s}_e}(\mathbf{v}) = \int_{I_{\mathbf{s}}} \int_{\phi(\mathbf{s}_e)} \bar{\mathbf{D}}_{ijkl} \frac{\partial \mathbf{v}_i}{\partial \mathbf{y}_j} \, d\mathbf{y} d\mathbf{s}_e,$$

in which $\bar{\mathbf{D}}$ is the elasticity tensor of the solid material, and $I_{\mathbf{s}} = I_1 \times I_2 \times \cdots \times I_m$ is the range of the shape parameter $\mathbf{s}_e = (s_1, s_2, \cdots, s_m)$, without considering the interconnection of solid elements or pores in this case. For example, $\mathbf{s}_e = (s_1, s_2, s_3) = (a_e, b_e, c_e)$ for an ETPMS element.

In our PGD-based approach, each parametric displacement field $\boldsymbol{\mu}^{kl}(\mathbf{y}, \mathbf{s}_e)$ is to be approximated as a sum of the products of decomposed functions in the following form:

$$\boldsymbol{\mu}^{kl}(\mathbf{y}, \mathbf{s}_e) \approx \sum_{i=1}^{M} (\bar{\boldsymbol{\mu}}^{kl})^i(\mathbf{y}, \mathbf{s}_e), \quad \text{for} \quad (\bar{\boldsymbol{\mu}}^{kl})^i(\mathbf{y}, \mathbf{s}_e) := \mathbf{d}^i(\mathbf{y}) g_1^i(s_1) g_2^i(s_2) \cdots g_m^i(s_m), \tag{24}$$

where $\mathbf{d}^i(\mathbf{y})$ is a piecewise polynomial function of the spatial coordinate $\mathbf{y}$, and each $g_j^i(s_j) \in \mathcal{L}^2(I_j)$ is a function of the parameter $s_j \in I_j$. The corresponding test function $\mathbf{v}$ in (23) is also represented in the separated form as in (24).

Accordingly, the parametric homogenization approach consists of two main steps:

1. Solve (23) *offline* to obtain the parametric displacement fields $\boldsymbol{\mu}^{kl}(\mathbf{y}, \mathbf{s}_e)$.
2. Compute *online* to obtain $\mathbf{D}^H(\mathbf{s}_e^0)$ for a certain shape parameter $\mathbf{s}_e^0$, by substituting $\boldsymbol{\mu}^{kl}(\mathbf{y}, \mathbf{s}_e^0)$ into (19).

The successful derivation of the solution to (23) must overcome two main challenges: conducting FE analysis on the varied domain $\phi(\mathbf{s}_e)$, and an efficient numerical approach for computing the PGD solution in the form given in (24). Numerical approaches for addressing these two issues are explained in the following.

5.2. Conversion from varied domain to fixed domain

The solution $\boldsymbol{\mu}^{kl}(\mathbf{y}, \mathbf{s}_e)$ to (24) is defined over a varied computational domain $\phi(\mathbf{s}_e)$, and a classical approach would involve a costly repeating re-meshing process. We resolve this issue by converting the varied domain $\phi(\mathbf{s}_e)$ into a fixed domain using the characteristic function. Specifically, we rewrite (23) in the following equivalent form:

$$A_{\mathbf{s}_e}(\boldsymbol{\mu}^{kl}, \mathbf{v}) = L_{\mathbf{s}_e}(\mathbf{v}), \tag{25}$$

where

$$A_{\mathbf{s}_e}(\boldsymbol{\mu}^{kl}, \mathbf{v}) = \int_{I_{\mathbf{s}}} \int_{\Omega_e} H(\phi(\mathbf{y}, \mathbf{s}_e)) \cdot \bar{\mathbf{D}}_{ijpq} \frac{\partial \boldsymbol{\mu}_p^{kl}}{\partial \mathbf{y}_q} \frac{\partial \mathbf{v}_i}{\partial \mathbf{y}_j} \, d\mathbf{y} d\mathbf{s}_e,$$

$$L_{\mathbf{s}_e}(\mathbf{v}) = \int_{I_{\mathbf{s}}} \int_{\Omega_e} H(\phi(\mathbf{y}, \mathbf{s}_e)) \cdot \bar{\mathbf{D}}_{ijkl} \frac{\partial \mathbf{v}_i}{\partial \mathbf{y}_j} \, d\mathbf{y} d\mathbf{s}_e,$$

in which H is the Heaviside function, and in practice, it is replaced by its regularized version as

$$H(\phi(\mathbf{y}, \mathbf{s}_e)) = \begin{cases} 1, & \phi(\mathbf{y}, \mathbf{s}_e) > \gamma, \\ \frac{3(1-\varepsilon)}{4}\left(\frac{\phi}{\gamma} - \frac{\phi^3}{3\gamma^3}\right) + \frac{(1+\varepsilon)}{2}, & -\gamma \le \phi(\mathbf{y}, \mathbf{s}_e) \le \gamma, \\ \varepsilon, & \phi(\mathbf{y}, \mathbf{s}_e) < -\gamma, \end{cases} \tag{26}$$

where γ is a small-valued parameter that controls the magnitude, and ε is a small positive number to prevent singularity of the global stiffness matrices during FE analysis. We use $\gamma = 0.005$ and $\varepsilon = 10^{-9}$ in this study.

Although $\boldsymbol{\mu}^{kl}$ and $\mathbf{v}$ can be represented as the separated form as in (24), the integration function in (25) must be computed in the high-dimensional space $\Omega_e \times I_{\mathbf{s}}$ because H is a function with respect to all $\mathbf{y}$ and s_j, $j = 1, ..., m$. This requires excessive time because of the curse of dimensionality, which can be resolved by separating the variables $\mathbf{x}$ and s_j in the characteristic function H, thereby yielding H in the following separated form:

$$H(\phi(\mathbf{y}, \mathbf{s}_e)) \approx \sum_i H_{\mathbf{y}}^i(\mathbf{y}) H_{s_1}^i(s_1) H_{s_2}^i(s_2) \cdots H_{s_m}^i(s_m). \tag{27}$$

The separation of the characteristic function H can be achieved using high-order singular-value decomposition (HOSVD) [33], as explained below. Thereafter, the variables are separated in the integral in (25) and the high-dimensional integration is to be computed as the sum of products of certain low-dimensional integrations, which incurs substantially lower computational costs.

5.3. Variable decomposition of characteristic function

Let χ denote a variable in $\{x, y, z, s_1, \ldots, s_m\}$, and we sample n_χ points for each variable χ. Consequently, we have a total of $\prod_{p\in P} n_p$ points in the domain $e \times I_{s_1} \times \cdots \times I_{s_m}$, which yields a tensor $\mathcal{H} \in \mathbb{R}^{n_x \times n_y \times n_z \times n_{s_1} \times \cdots \times n_{s_m}}$ computed via

$$\mathcal{H}_{i_1,i_2,i_3,i_4,\cdots,i_{m+3}} = H(x_{i_1}, y_{i_2}, z_{i_3}, s_{1_{i_4}}, \cdots, s_{m_{i_{m+3}}}). \tag{28}$$

HO-SVD aims to approximate the function H as products of functions in a lower dimension by approximating its values at these sample points of tensor $\mathcal{H}$. Specifically, it first approximates $\mathcal{H}$ in the following Tucker product form:

$$\mathcal{H} \approx \mathcal{S} \times_1 U^x \times_2 U^y \times_3 U^z \times_4 U^{s_1} \times_5 \cdots \times_{m+3} U^{s_m}, \tag{29}$$

where $\mathcal{S}$, with size $k_1 \times k_2 \times \cdots k_{m+3}$, is the core, and each $U^{(\chi)} \in \mathbb{R}^{n_\chi \times k_\chi}$ is the matrix corresponding to the variable χ.

Let $\overline{U}_i^\chi$ be the approximate function in terms of one-dimensional linear FE bases and U_i^χ be the i-th coefficient column vector of U^χ for $i = i_1, \ldots, i_{m+3}$. Thus, we have the following decomposed form approximating H:

$$H \approx \sum_{i_1=1}^{k_1} \cdots \sum_{i_{m+3}=1}^{k_{m+3}} s_{i_1,\cdots,i_{m+3}} \overline{U}_{i_1}^x(x)\overline{U}_{i_2}^y(y)\overline{U}_{i_3}^z(z)\overline{U}_{i_4}^{s_1}(s_1)\cdots\overline{U}_{i_{m+3}}^{s_m}(s_m). \tag{30}$$

Algorithm 1 Numerical approach for PGD.

Initialize Set the solution $\boldsymbol{\mu} = \mathbf{0}$, iteration step N=0, approximation error *err_iter*=1, and provide the maximal iteration step *max_iter* and tolerance error *tol*.
while *err_iter* > *tol* and $N <$ *max_iter* **do**
  $N = N + 1$ //Increase the iteration step.
  Initialize Set $\mathbf{d} = \mathbf{0}$, $g_j = \mathbf{1}$, $j = 1, \cdots, m$, and the error $err = 1$.
  while *err* > *tol* **do**
    $\mathbf{d}^r = \mathbf{d}$, $g_j^r = g_j$, $j = 1, \cdots, m$ // Record the origin values for the fixed-point check.
    Find $\mathbf{d}$ for all $\delta\mathbf{d}$ such that

$$A(\mathbf{d}\prod_{j=1}^{m} g_j) = L(\delta\mathbf{d}\prod_{j=1}^{m} g_j) - A(\boldsymbol{\mu}^{N-1}, \delta\mathbf{d}\prod_{j=1}^{m} g_j).$$

    Find g_k $(k = 1, \cdots, m)$ sequentially for all corresponding δg_k such that

$$A(\mathbf{d}\prod_{j=1}^{m} g_j) = L(\mathbf{d}\delta g_k\prod_{j\neq k} g_j) - A(\boldsymbol{\mu}^{N-1}, \mathbf{d}\delta g_k\prod_{j\neq k} g_j).$$

    $err = ||\mathbf{d}^r - \mathbf{d}|| + \sum_{j=1}^m ||g_j^r - g_j||$ //Check if the fixed point is reached.
  end while
  $\boldsymbol{\mu} = \boldsymbol{\mu} + \mathbf{d}\prod_{j=1}^m g_j$. //Enrich the solution.
  $err\_iter = ||\mathbf{d}|| \cdot \prod_{j=1}^m ||g_j||$ //Check if the solution converge.
end while
Return $\boldsymbol{\mu}$.

5.4. Numerical solution of PGD

Each parametric displacement field $\boldsymbol{\mu}^{kl}(\mathbf{y}, \mathbf{s}_e)$ is to be approximated using the PGD form as in (24). For simplicity, the superscript of $\boldsymbol{\mu}^{kl}(\mathbf{y}, \mathbf{s}_e)$ is abbreviated; that is, $\boldsymbol{\mu}^{kl}(\mathbf{y}, \mathbf{s}_e)$ is represented as $\boldsymbol{\mu}(\mathbf{y}, \mathbf{s}_e)$.

The computation of PGD solution (24) can be achieved by an enrichment process together with a fixed-point strategy following [15]. Specifically, we determine the solution in the i-th step using the results from $(i-1)$-th step in the following form:

$$\boldsymbol{\mu}^{(i)}(\mathbf{y}, \mathbf{s}_e) = \boldsymbol{\mu}^{(i-1)}(\mathbf{y}, \mathbf{s}_e) + \mathbf{d}(\mathbf{y})\prod_{j=1}^{m} g_j(s_j), \tag{31}$$

where $\mathbf{d}(\mathbf{y})$ and $g_j(s_j)$ $(j = 1, \ldots, m)$ are to be determined in the i-th enrichment procedure.

Substituting (31) into (23) results in

$$A(\mathbf{d}\prod_{j=1}^{m} g_j, \mathbf{v}) = L(\mathbf{v}) - A(\boldsymbol{\mu}^{(i-1)}, \mathbf{v}), \tag{32}$$

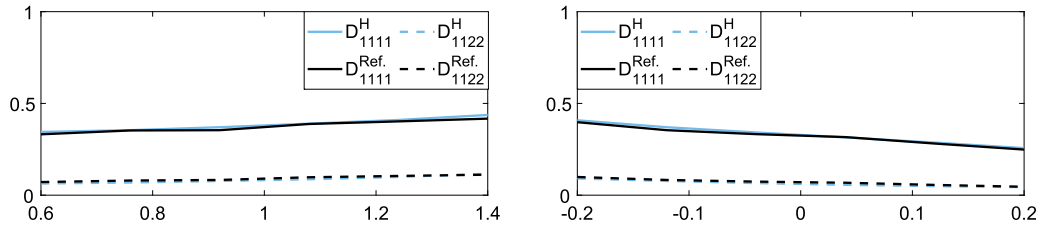

(a) varied b when $a = 1, c = -0.12$ (b) varied c when $a = 1, b = 0.92$

Fig. 11. Comparison between components of elasticity tensors computed via our parametric homogenization approach *without using HO-SVD* and via the numerical homogenization approach for the ETPMS element.

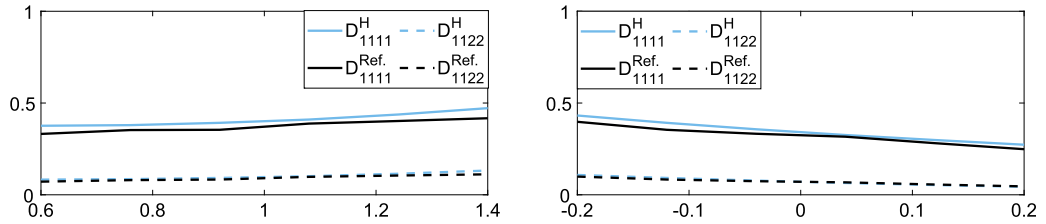

(a) varied b when $a = 1, c = -0.12$ (b) varied c when $a = 1, b = 0.92$

Fig. 12. Comparison between components of elasticity tensors computed via our parametric homogenization approach *using HO-SVD* and via the numerical homogenization approach for the ETPMS element.

where the test function $\mathbf{v}$ is also separated as,

$$\mathbf{v} = \delta\mathbf{d}\prod_{j=1}^{m} g_j + \sum_{k=1}^{m} \mathbf{d}\delta g_k \prod_{j=1, j\neq k}^{m} g_j, \tag{33}$$

in which $\delta\mathbf{d}$ and δg_k are test functions for $\mathbf{d}$ and $g_k(\ k = 1, \ldots, m)$, respectively.

An iterative fixed-point procedure is applied for each enrichment step to compute $\mathbf{d}$ and $g_k,\ k = 1, \ldots, m$ iteratively, one by one, by fixing the values of the other functions. The pseudo-code of the numerical approach for PGD is presented in Algorithm 1.

5.5. Performance of parametric homogenization

The proposed PGD-based parametric homogenization approach was implemented in MATLAB 2018b, and run on a PC with a 3.6 GHz Intel Core i7 CPU and 16 GB RAM. On this basis, the efficiency and accuracy of the parametric homogenization were analyzed for a base material with Young's modulus $E = 1$ Pa and Poisson's ratio $\nu = 0.33$.

We first investigate the computational efficiency. Consider a specific case, in which we computed a five-term PGD solution for an ETPMS element with parameters $a, b \in (0.6, 1.4)$ and $c \in (-0.2, 0.2)$. This required 4.2 and 8.7 h with or without using HO-SVD, respectively. Thereafter, evaluating the effective elasticity tensor (19) only took an average of 0.04 s. For comparison, directly performing the numerical homogenization was estimated to take approximately 694 h, or approximately 29 days for a sample of $50 \times 50 \times 200$ or a total of 5×10^5 points (a_e, b_e, c_e); each sample took approximately 5.16 s for an ETPMS with a mesh size of $20 \times 20 \times 20$.

The computational accuracy was also analyzed for a set of sampling points by comparing the obtained homogenized elasticity tensors using our approach with or without HO-SVD against those obtained using numerical homogenization, measured in terms of their Euclidean distance. High approximation accuracy was observed, even when using HO-SVD approximation, where the relative errors were always below 6%. Figs. 11 and 12 also show the results at certain sampling points. Note that, in this example, only a five-term PGD solution was computed under the computational budget. Higher-order approximation accuracy is expected to be achieved when using more PGD terms.

6. Numerics behind optimization

The modeling advantages of the ETPMS come at the cost of challenges in terms of its efficient optimization of Problem P_D in Eq. (15) owing to its implicitly defined and varied computational domain and the large number of validity constraints on the ETPMS cells. A numerical approach for resolving this issue is explained in this section.

6.1. Optimization approach

First, consider the connection constraint of the solid or/and porous regions for an ETPMS, as stated in Lemma 1 and indicated by P_D in Eq. (15):

$$\mathbf{s}_e \in I^s, \quad \text{or} \quad \mathbf{s}_e \in I^{sp}.$$

We rewrite the constraints as follows for ease of explanation:

$$0 \le \bar{g}_{e,i}(a,b,c) \le \alpha, \quad 1 \le i \le l,\ 1 \le e \le N,$$

or

$$\mathbf{0} \le \bar{\mathbf{g}} \le \boldsymbol{\alpha},$$

where $l = 4$ or 7 is the constraint number for an ETPMS element in Lemma 1.

The per-element validity requirement involves numerous constraints, and thus, the associated optimization problem (15) is very challenging to compute efficiently. In fact, we can reduce the large number of constraints into a single equivalent one as follows:

$$\max \bar{\mathbf{g}} = \max_{1\le i\le l,\ 1\le e\le N} (\bar{g}_{e,i}) \le \alpha.$$

Considering that the max function is not differentiable, we approximate it further using the p-norm function

$$\max \bar{\mathbf{g}} = \max_{1\le i\le l,\ 1\le e\le N} (\bar{g}_{e,i}) \approx \|\bar{\mathbf{g}}\|_p = (\sum (\bar{g}_{e,i})^p)^{\frac{1}{p}},$$

and $\|\bar{\mathbf{g}}\|_p$ approaches $\max \bar{\mathbf{g}}$ as p goes to infinity.

To account for the difference between $\max \bar{\mathbf{g}}$ and $\|\bar{\mathbf{g}}\|_p$ when the value of p is not infinitely large, we further rewrite the consolidated constraint $\max \bar{\mathbf{g}} \le \alpha$ as

$$(\sum (\bar{g}_{e,i})^p)^{\frac{1}{p}} \le (\sum \alpha^p)^{\frac{1}{p}},$$

which can be re-arranged as

$$(\frac{1}{lN} \sum_{1\le i\le l,\ 1\le e\le N} (\bar{g}_{e,i})^p)^{\frac{1}{p}} \le \alpha,$$

where N is the number of elements, $l = 4$ or 7 is the constraint number for an ETPMS element involved in Lemma 1. Specifically, $l = 4$ if only the interconnection of the solid part is required, or $l = 7$ if the interconnection of both the solid part and the void part is required.

A larger p enforces the per-element constraints more strictly, while simultaneously increasing the nonlinearity of the problem. When a too-small p is taken, the optimization may converge to a result where the interconnection constraints are not satisfied for a few elements. On the other hand, when a too-large p is taken, the optimization may fail to reach a converged result. In our examples, we set $p = 64$ after testings, which is large enough to keep the interconnection constraints for all elements and simultaneously the optimization reach good convergency. Consequently, we obtain the following consolidated optimization problem.

The optimization problem in (15) is reformulated in the following form using a p-norm: find the design variables $\mathbf{s} = \{\mathbf{s}_e\} \in \mathbb{R}^{N\times 3}$ satisfying

$$(\textbf{Problem}: P_p) \qquad \min_{\mathbf{s}\in\mathbb{R}^{N\times 3}} C(\mathbf{u},\mathbf{s}), \text{ compliance minimization},$$

$$\text{s.t.} \quad \begin{cases} \mathbf{K}(\mathbf{s})\mathbf{u} = \mathbf{f},\ \mathbf{u} \in \mathbb{R}^n, & \text{equilibrium equation}, \\ \frac{V(\mathbf{s})}{|\Omega|} \le \mathcal{V}, & \text{volume fraction constraint}, \\ (\frac{1}{lN}\sum (\bar{g}_{e,i})^p)^{\frac{1}{p}} \le \alpha, & \text{interconnection constraint}. \end{cases} \tag{34}$$

The solution is computed using the classical optimization approach GCMMA [34,35].

6.2. Offline pre-computations

Even with the offline PGD-based parametric homogenization, the computational costs remain very intensive as various function integrations are involved, particularly in computing the effective elasticity tensor and stiffness matrix for each ETPMS element. These computations are called up to millions of times during all optimization iterations. They are further accelerated by means of the strategy of offline pre-computation and online interpolation.

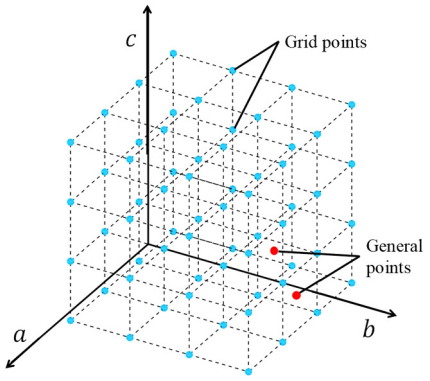

Fig. 13. The values of the elasticity tensors and their derivatives at the grid points are pre-computed in the parameter space. Their values at a general point are interpolated during optimization.

Elasticity tensor $\mathbf{D}^H_{ijkl}$ pre-computation The elasticity tensor $\mathbf{D}^H_{ijkl}(\phi(\mathbf{s}_e))$ is defined by (19); that is,

$$\mathbf{D}^H_{ijkl}(\phi(\mathbf{s}_e)) = \frac{1}{|\Omega_e|}\int_{\Omega_e}(H(\phi(\mathbf{s}_e))\cdot\bar{\mathbf{D}}_{ijkl}(\phi(\mathbf{s}_e),\mathbf{y}) - H(\phi(\mathbf{s}_e))\cdot\bar{\mathbf{D}}_{ijpq}(\phi(\mathbf{s}_e),\mathbf{y})\frac{\partial\boldsymbol{\mu}^{kl}_p}{\partial\mathbf{y}_q})d\mathbf{y}. \tag{35}$$

In spite of the solution $\boldsymbol{\mu}^{kl}_p$ being obtained in the PGD form as in Eq. (24), the integration in $\mathbf{D}^H_{ijkl}$ involves the varied domain $\phi(\mathbf{s}_e)$ or its associated Heaviside function, and must be numerically conducted with un-ignorable efforts using, for example, Gaussian integration. Conducting the integration millions of times is highly intensive. In our pre-computation strategy, we first evenly sample a set of points within the range $I = I^s$ or I^{sp} provided in Lemma 1, and subsequently compute the values of the tensors $\mathbf{D}^H_{ijkl}(\phi(\mathbf{s}_e))$ on the grid points. The tensor values on the other points are then evaluated by interpolation, as illustrated in Fig. 13.

Stiffness matrix $\mathbf{K}_e(\mathbf{s}_e)$ pre-computations The stiffness matrix for an ETPMS element is defined by (16),

$$\mathbf{K}_e(\mathbf{s}_e) = \int_{\Omega_e}\mathbf{B}^T\mathbf{D}^H(\mathbf{s}_e)\mathbf{B}\,dV. \tag{36}$$

Note that each Ω_e is a $1\times1\times1$ cubic cell and $\mathbf{B}$ is the same for all such integrations via mapping Ω_e to $[0,1]^3$. Thus we obtain

$$\int_{[0,1]^3}\mathbf{B}^T\mathbf{D}^H(\mathbf{s}_e)\mathbf{B}\,dV = \sum_{i=1,j=1}^{i=6,j=6}\mathbf{D}^H_{i,j}(\mathbf{s}_e)\int_{[0,1]^3}\mathbf{B}^T_i\mathbf{B}_j\,dV, \tag{37}$$

where $\mathbf{D}^H_{i,j}(\mathbf{s}_e)$ is the i-th row, j-th column element of the matrix form of $\mathbf{D}^H(\mathbf{s}_e)$, and $\mathbf{B}_i$ is the i-th row of $\mathbf{B}$.

In this manner, we pre-compute $\int_{[0,1]^3}\mathbf{B}^T_i\mathbf{B}_j\,dV$ offline for $i=1,\dots,6,\ j=1,\dots,6$ such that the integrations over the cubic unit cell can be efficiently computed via (37).

6.3. Sensitivity computation

A key process in computing the solution to the optimization problem P_p in Eq. (34) is determining the sensitivities of the objective function and the volume fraction and connection constraints with respect to the design variables. These are derived as follows.

As the shape parameters only affect the corresponding ETPMS element, we first obtain

$$\frac{\partial\mathbf{K}_i(\mathbf{s}_i)}{\partial s_e} = 0,\ \frac{\partial V(\mathbf{s}_i)}{\partial s_e} = 0,\ \text{if } i\neq e, \tag{38}$$

where s_e represents one of the design variables a_e, b_e, c_e of an ETPMS element associated with the unit cell Ω_e.

Using the adjoint method [36], the sensitivity of the objective function is determined as

$$\frac{\partial C}{\partial s_e} = -\frac{\partial}{\partial s_e}\sum_{i=1}^{N}\mathbf{u}_i^T\mathbf{K}_i(\mathbf{s}_i)\mathbf{u}_i = -\sum_{i=1}^{N}\mathbf{u}_i^T\frac{\partial\mathbf{K}_i(\mathbf{s}_i)}{\partial s_e}\mathbf{u}_i = -\mathbf{u}_e^T\frac{\partial\mathbf{K}_e(\mathbf{s}_e)}{\partial s_e}\mathbf{u}_e, \tag{39}$$

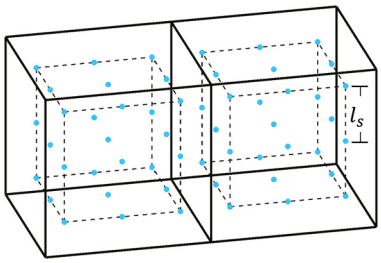

Fig. 14. Selected interpolation points for smoothing adjacent ETPMS elements used to construct c-ETPMS from set of discrete ETPMS elements.

where

$$\frac{\partial \mathbf{K}_e(\mathbf{s}_e)}{\partial s_e} = \frac{\partial}{\partial s_e}\int_{\Omega_e} \mathbf{B}^T \mathbf{D}^H(\mathbf{s}_e)\mathbf{B}\, dV = \int_{\Omega_e} \mathbf{B}^T \frac{\partial \mathbf{D}^H(\mathbf{s}_e)}{\partial s_e}\mathbf{B}\, dV. \tag{40}$$

The sensitivity of the effective elasticity tensor can also be derived analytically following a similar concept to that in [37],

$$\frac{\partial \mathbf{D}^H_{ijkl}(\Omega_e)}{\partial s^e} = -\frac{1}{|\Omega_e|}\int_{\Omega_e}\left(\mathbf{e}_i \bigotimes \mathbf{e}_j - \frac{\partial \boldsymbol{\mu}^{ij}}{\partial \mathbf{y}}\right)\frac{\partial H(\phi(\mathbf{y},\mathbf{s}_e))}{\partial s^e}\overline{\mathbf{D}}\left(\mathbf{e}_k \bigotimes \mathbf{e}_l - \frac{\partial \boldsymbol{\mu}^{kl}}{\partial \mathbf{y}}\right) d\mathbf{y}, \tag{41}$$

where $\mathbf{e}_i$, $\mathbf{e}_j$, $\mathbf{e}_k$ and $\mathbf{e}_l$ are unit basis vectors and $\bigotimes$ denotes the tensor product.

Note that the above equation involves the gradients of the Heaviside function $H(\phi(\mathbf{y},\mathbf{s}_e))$, specifically its regularized smooth version defined in Eq. (26). The integration must be conducted numerically using an extremely fine sampling of Gaussian points, which is computationally expensive. In our numerical examples, we compute these values from the offline computed $\mathbf{D}^H$ in Section 6.2 instead.

Moreover, the sensitivity of the volume constraint is determined as

$$\frac{\partial V}{\partial s_e} = \frac{\partial}{\partial s_e}\sum_{i=1}^{N} V(\mathbf{s}_i) = \sum_{i=1}^{N}\frac{\partial V(\mathbf{s}_i)}{\partial s_e} = \frac{\partial V(\mathbf{s}_e)}{\partial s_e}. \tag{42}$$

The element volume $V(\mathbf{s}_e)$

$$V(\mathbf{s}_e) = \int_{\Omega_e} H(\phi(\mathbf{y},\mathbf{s}_e))\, d\mathbf{y}, \tag{43}$$

can be computed efficiently by determining the relative location (interior or exterior) of the sampling Gaussian points, of a specific number 200^3 in our case, with respect to an ETPMS element $\phi(\mathbf{s}_e)$ by evaluating the values of the associated implicit function at these points. Similarly, the sensitivities are pre-computed on a set of sampled grid points. Their values on the other points are evaluated by means of online interpolation.

The sensitivity of the connection constraint is straightforward to derive and is not explained further here.

6.4. Smoothness between adjacent elements

The optimization process described above generates a set of discrete optimized ETPMS elements determined by the parameters $\mathbf{s}_e = \{(a_e, b_e, c_e)\}$. To enable a smooth transition between the adjacent ETPMS elements, the parameter functions $a(\mathbf{x}), b(\mathbf{x}) and c(\mathbf{x})$ are further constructed, each of which interpolates the discrete control parameters $\{a_e\}$, $\{b_e\}$, and $\{c_e\}$, respectively. Existing interpolation techniques include radial basis function interpolation, the natural neighbor approach, and linear interpolation. The natural neighbor approach with C^1 continuity is applied in this case. Meanwhile, to preserve the shapes of the optimized pore structures, 27 interpolation points are selected from each cell, as illustrated in Fig. 14. These points are generated from a cube with size $2l_s$, where l_s is a positive real value close to but less than 0.5.

Fig. 15 presents the generated structures before and after the smoothing operation for $l = 0.49$ of a specific parameter c. A small difference in the structural appearance and parameter distribution can be observed.

A parameter shape filter, which is commonly applied in topology optimization [36], is also used in this case to smooth the variations between adjacent ETPMS elements at each optimization iteration. The filter updates the shape parameter as the weighted average of the adjacent shape parameters to prevent abrupt changes. In particular, the filter operates by modifying the design variables as

$$\tilde{s_e} = \frac{\sum_{i\in N_e}\omega_{ie} s_i}{\sum_{i\in N_e}\omega_{ie}}, \tag{44}$$

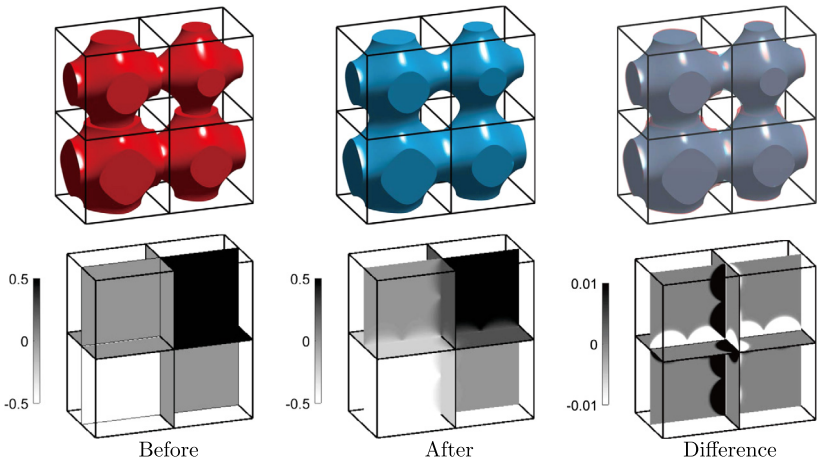

Fig. 15. Porous structures (first row) and associated distributions of shape parameter c (second row) before/after smoothing and their difference.

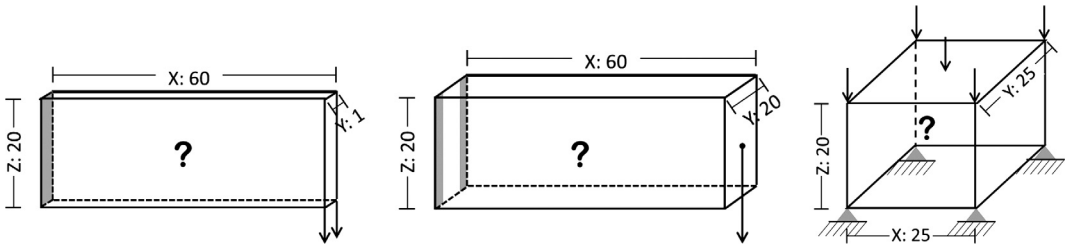

(a) Single-layer cantilever beam with unit force on edge.

(b) Multilayer beam with unit force on point.

(c) Multilayer table with unit force on face.

Fig. 16. Design domain and boundary conditions used in numerical tests.

where the weight ω_{ie} is expressed as

$$\omega_{ie} = r_{\min} - \text{dist}(\Omega_i, \Omega_e), \tag{45}$$

for the size of the neighborhood or filter $r_{\min}$, and N_e is the neighborhood of an element e, defined as

$$N_e = \{i \mid \text{dist}(\Omega_i, \Omega_e) \leq r_{\min}\}. \tag{46}$$

7. Numerical examples

The approach was implemented in MATLAB 2018b, and run on a PC with a 3.6 GHz Intel Core i7 CPU and 16 GB RAM. Its performance was tested in various cases, as outlined in this section. For all cases, the base material was assumed to have a Young's modulus of 1 Pa and Poisson's ratio of 0.33.

7.1. Overall performance: single-layer cantilever beam example

We first use the single-layer 3D cantilever beam example presented in Fig. 16(a) to demonstrate the performance of the approach in various aspects: its comparisons with the results from TPMS, ETPMS elements, and the classical SIMP-based topology optimization [38]; the overall optimization procedure; the performance in cases with different volume fractions; its hole size control ability; and the influence of the smoothing operations.

In this example, the fixed macro-design area consisted of $60 \times 1 \times 20$ cubic cells. Its left-side face was fixed and a vertical downward unit force $\mathbf{f}$ was imposed on the edge of the bottom-right corner. The target volume fraction $\mathcal{V} = 0.5$. The ranges of the parameters $c \in [-3, 1]$ for the TPMS element and $a, b \in [0.5, 2]$, $c \in [-5, 1]$ for the ETPMS element if not explicitly explained. A filter of size $r_{\min} = 1.5$ was used for all examples. The solid connection was required, while pore connections were ignored in this example.

Overall performance The computational results are presented in Fig. 17, including the generated c-ETPMS porous structures, benchmark SIMP-based topology optimization [38], TPMS-based structures, gray topology optimization obtained by setting the penalty power to 1, and its solid-void counterpart.

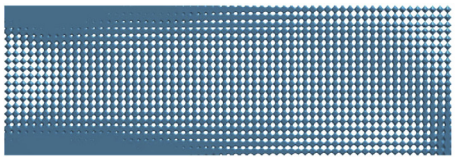

(a) Extended P element from (34); C: 769.63, SA: 3325.67, T: 19.27s (68 iterations).

(b) Compliance distribution for (a).

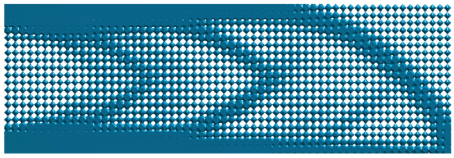

(c) P element; C: 796.68, SA: 2872, T: 82.06s (117 iterations).

(d) Compliance distribution for (c).

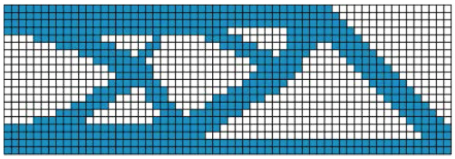

(e) Topology optimization; C: 807.66, SA: 1642, T: 14.60s (92 iterations).

(f) Compliance distribution for (f).

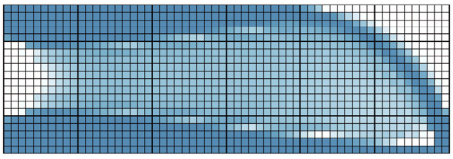

(g) Gray topology optimization; C: 637.94, T: 29.67s (173 iterations).

(h) Compliance distribution for (g).

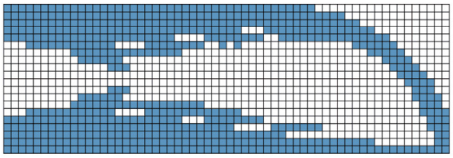

(i) Thresholding from (g); C: 2876.10.

(j) Compliance distribution for (i).

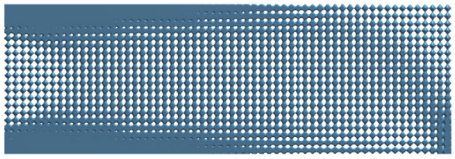

(k) Extended P element from (15); C: 771.06, SA: 3274.95, T: 1009.52s (29 iterations).

(l) Compliance distribution for (k).

Fig. 17. Results of single-layer cantilever beam case for various optimization approaches, where C: total compliance, SA: surface area, and T: computational time (iterations).

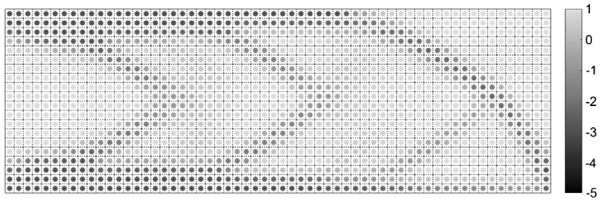

(a) P element

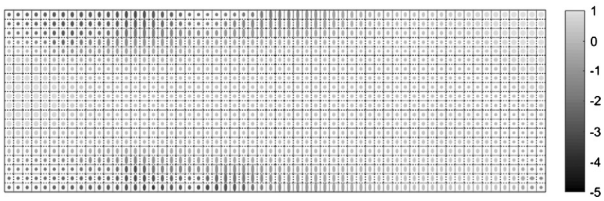

(b) Extended P element p-norm

Fig. 18. Distribution of shape parameters a, b, c of ETPMS elements, where the axes of the ellipses represent the values of the computed a, b along the horizontal and vertical directions, and the color represents the value of parameter c.

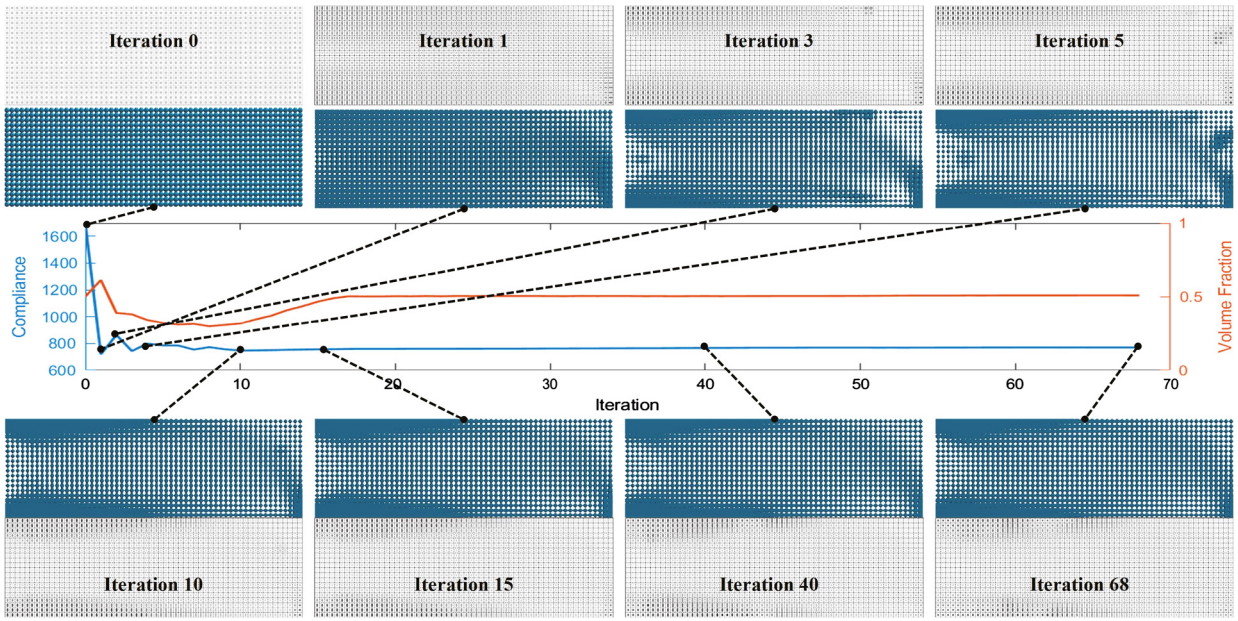

Fig. 19. Convergence curve in solving the optimization problem (34), where the large number of connection validity constraints is formulated into a single one using a p-norm formulation. It takes 68 iterations in 19.27 seconds to obtain an optimized heterogeneous porous structures.

As can be observed from the results, the ETPMS case exhibited smaller total compliance than the TPMS case, which were both inferior to that of the gray structure and superior to that of the solid-void structure obtained by topology optimization. Converting the gray structure into a solid-void one resulted in a significantly degrade structure. The phenomenon is reasonable, as the ETPMS element has more degrees of freedom than the TPMS element. However, as the design variable range is confined for solid connections, it consequently demonstrated inferior performance to the gray structure obtained from topology optimization.

In addition to the close compliance approximation, note that the ETPMS-based porous structures exhibit the unique merits of a smooth network and large open surface area to volume ratio, which are ideal for various medical or biological applications; for example, tissue engineering [6]. Moreover, similar to the truss- or lattice-like structures studied previously [9,10,12–14], the porous structures offer the advantage of improved buckling capabilities.

Fig. 18 also plots the distributions of the obtained parameters (a_e, b_e, c_e), where the elliptic hole axes indicate a, b values, and the color represents the value of c; see also Eq. (3). According to the figure, also the compliance distributions in Fig. 17, the per-element compliance/size variation of the ETPMS porous structure changed more smoothly than those of the TPMS structure or the structure obtained from topology optimization. This is believed to have resulted from the additional degrees of design freedom of the ETPMS elements with enhanced anisotropy. However, these different structures have similar overall compliance distributions as they all had to adapt to the stress distributions for performance optimization.

Optimization procedure The ETPMS-based porous structures can be obtained via computing solutions to problems (34) or (15) under a single consolidated constraint or a large number of constraints on connection validity. As previously shown in Figs. 17(a) and (k), both results produce reasonable ETPMS-based porous structures, and have close target total compliances. We further show here the procedures and intermediate results from the two approaches in Figs. 19 and 20. Both approaches iteratively improve the structural compliances until convergence. On the other hand, using the single consolidated constraint in (34) takes much less computational time, respectively taking 68 iterations, 19.27 seconds and 29 iterations and 1009.52 seconds, while simultaneously maintaining the connection requirement.

Different volume fractions The approach can also design heterogeneous porous structures at different volume fractions. Its performance was tested using volume fractions of $\mathcal{V} = 0.6$ and 0.7, as illustrated in Fig. 21. The approach was effective in both cases, and the larger volume fraction induced a structure with greater material occupation, and consequently, smaller overall compliance. In both cases, the total compliances of the obtained porous structures were less than those of the benchmark topology optimization results.

Hole size control The approach can control the pore sizes by specifying range of the design parameters $\{a_e, b_e, c_e\}$. It was tested for the following two cases:

Case 1: $a, b \in [0.8, 1.2],\ c \in [-3, 1]$;

Case 2: $a, b \in [0.8, 1.2],\ c \in [-3, 1]$ with an additional constraint on the pore connectivity.

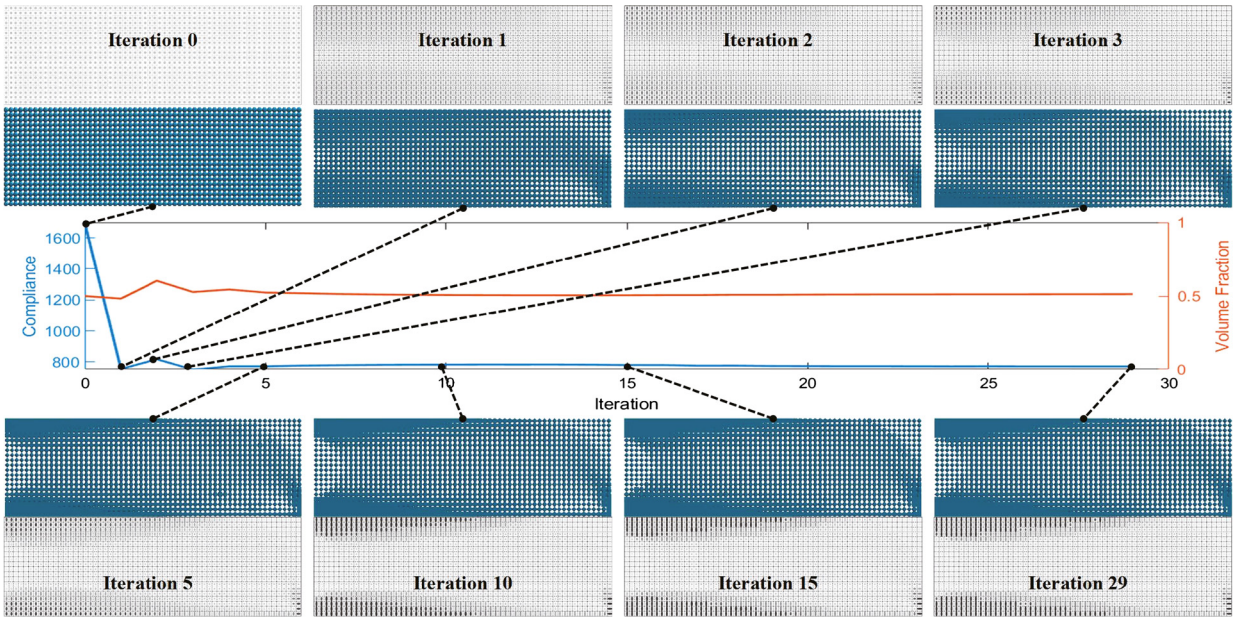

Fig. 20. Convergence curve in solving the optimization problem (15), under a large number of connection validity constraints. It takes 29 iterations in 1009.52 seconds to obtain an optimized heterogeneous porous structures.

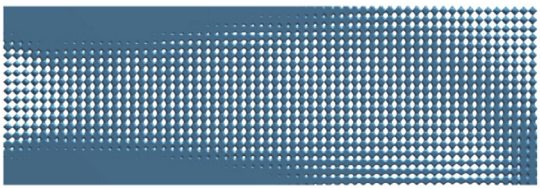

(a) Ours: $C = 654.02$ with $\mathcal{V} = 0.6$.

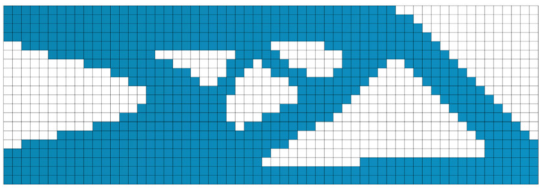

(b) Topology Optimization: $C = 676.14$ with $\mathcal{V} = 0.6$.

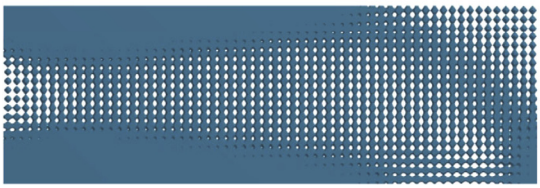

(c) Ours: $C = 568.62$ with $\mathcal{V} = 0.7$.

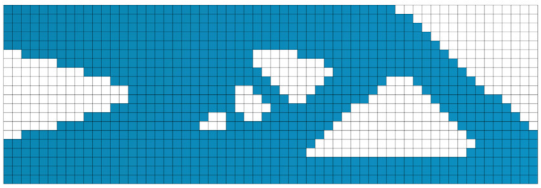

(d) Topology Optimization: $C = 588.66$ with $\mathcal{V} = 0.7$.

Fig. 21. Different optimized porous structures at different volume fraction constraints.

The obtained structures are depicted in Fig. 22. The stricter range produced a structure with inferior stiffness, or larger compliance, which was consistent with our intuition.

Influence of smoothing To determine the influence of the smoothing procedure after obtaining the discrete ETPMS, as described in Section 6, we compared the two structures and their properties before and after smoothing in further detail. The derived structures are first plotted in Fig. 23.

The computation is based on the homogenization theory, as described in Lemma 2, which assumes periodicity of the studied microstructure. However the symmetry of the boundary is no longer satisfied here due to the smoothing procedure. The following *asymmetric index* is first introduced to measure the asymmetry of a microstructure's boundary, along the X-direction,

$$\frac{\int_{\Gamma_e^X} |H(\phi(x,y,z,\mathbf{s}(x,y,z))) - H(\phi(x',y,z,\mathbf{s}(x',y,z)))|\, dydz}{\int_{\Gamma_e^X} dydz}, \tag{47}$$

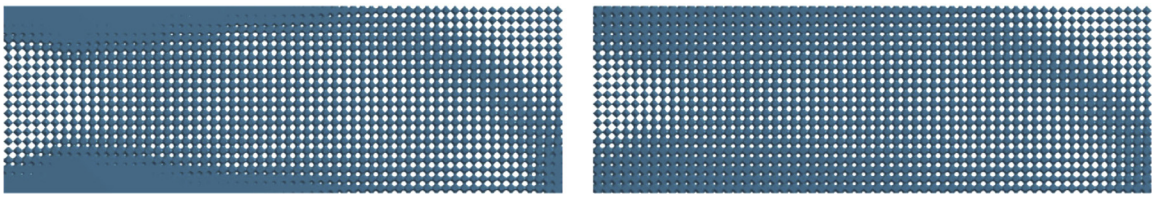

(a) $C = 824.95$, with $0.8 \leq a, b \leq 1.2$, $-3 \leq c \leq 1$ and constraint on interconnection of solid part.

(b) $C = 976.72$, with $0.8 \leq a, b \leq 1.2$, $-3 \leq c \leq 1$ and constraint on interconnection of solid and porous parts.

Fig. 22. Different optimized porous structures were produced when constraints on the solid and pore connectivity were respectively prescribed.

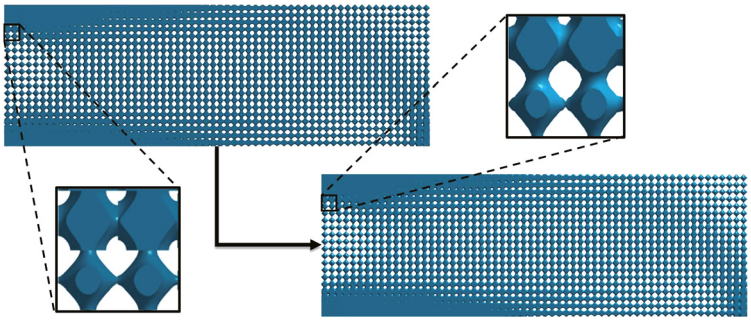

Fig. 23. Optimized ETPMS-based porous structures before and after smoothing.

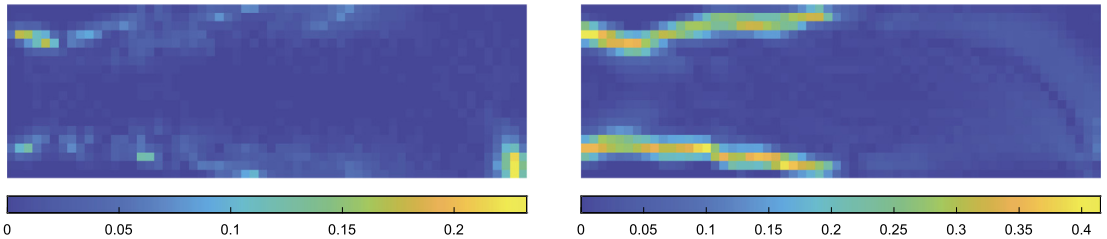

(a) X-direction. Mean = 1.17%

(b) Z-direction. Mean = 4.56%

Fig. 24. Distributions of asymmetry indexes of microstructures in the smoothed porous structure.

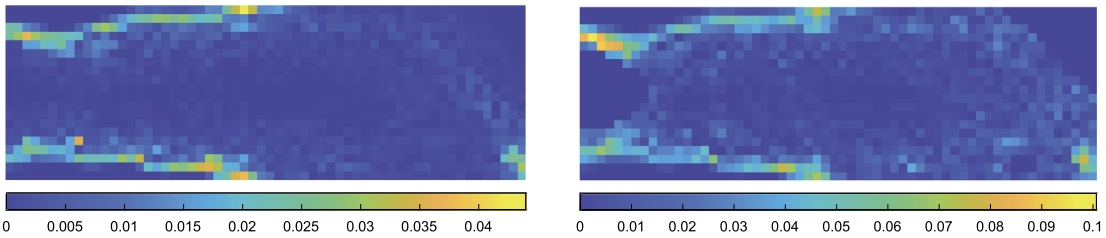

(a) D^H_{11}. Mean = 0.34%

(b) Trace of D^H. Mean = 0.99%

Fig. 25. Distributions of relative errors of effective elasticity tensors before and after smoothing.

where Γ_e^X is one boundary face of Ω_e perpendicular to X-axis, and (x', y, z), $(x, y, z) \in \Gamma_e^X$ are the associated symmetric point pair.

The asymmetric index along the Y- or Z-direction is similarly defined. Fig. 24(a), (b) respectively shows the distribution of the asymmetric index along the X- or Z-direction of the smoothed optimal porous structure, whose mean values are 1.17% and 4.56% respectively. The porous structure has one single layer and is symmetric along the Y-direction.

The effective elasticity tensor for each microstructure is computed via numerical homogenization, either before or after smoothing, and their relative difference is illustrated in Fig. 25. We also show in Fig. 26 the per-element compliance or volume difference before and after smoothing. Close approximation between the results is observed, demonstrating the ability to maintain the structural properties.

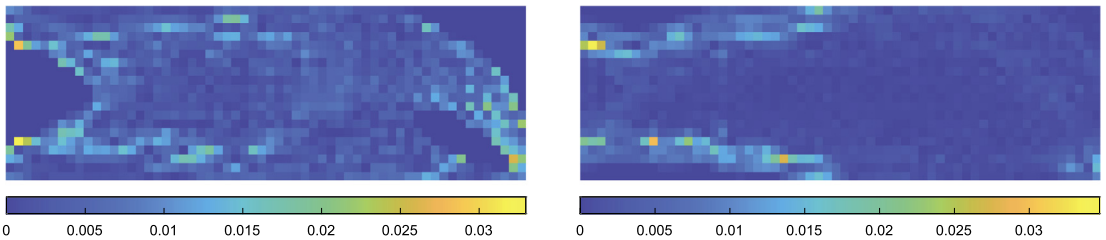

(a) Compliance. Mean = 0.40%

(b) Volume. Mean = 0.24%

Fig. 26. Distributions of relative errors of compliances and volumes before and after smoothing.

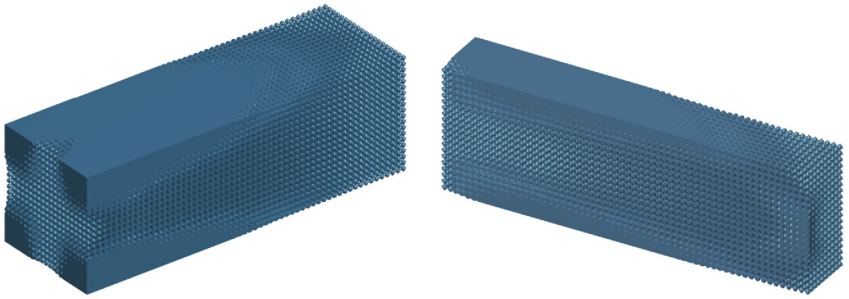

(a) Our approach: 10.38 total compliance, 1207 s, 73 iterations.

(b) Slice of result from our approach.

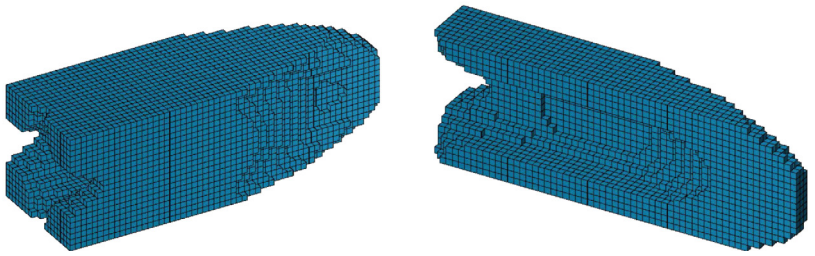

(c) Topology optimization: 10.67 total compliance, 857 s, 200 iterations.

(d) Slice of topology optimization result.

Fig. 27. Comparisons between optimized ETPMS-based porous structure and structure obtained from the traditional topology optimization for multilayer beam example in Fig. 16(b).

7.2. Further examples

We also tested the performance of the approach in relatively large design domains using the multilayer beam example and table example in Figs. 16 (b) and (c), respectively, both at a target volume fraction of 0.5. The boundary conditions of the multilayer beam example were specifically designed to produce an optimized structure with different layer configurations.

The optimized structures of the two examples are presented in Figs. 27 and 28 respectively, with their compliances and computational times indicated below the figures. For the table example in Fig. 28, our approach and the topology optimization produced structures with compliances of 7.24×10^5 and 7.26×10^5, respectively. The former yielded a superior structure of smaller compliance. This demonstrates the ability of the ETPMS-based approach to maintain the physical properties, while simultaneously generating interconnected heterogeneous porous structures.

8. Conclusions and future work

In this study, the concept of ETPMS was introduced to model heterogeneous and anisotropic porous structures via an implicit function of additional shape control parameters. The concept results in a perfectly smooth and fully connected porous network, but also comes at the cost of challenges in the effective simulation and optimization. We further resolved these issues using a combination of offline and online computations, particularly by using a PGD-based offline parametric homogenization technique and some carefully designed optimization techniques. Various numerical examples also demonstrated the performance of the approach in producing physically optimized heterogeneous interconnected porous structures.

However, this study exhibits several limitations, which are to be improved in the future. First, the offline parametric homogenization constructed on PGD requires substantial implementation efforts, and its associated sensitivity analysis is

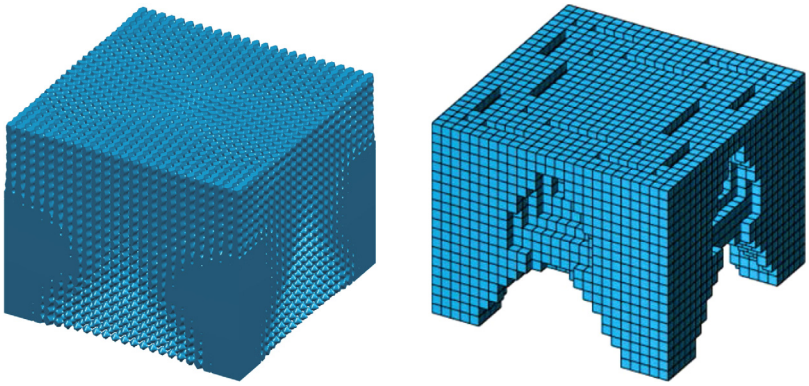

(a) Our approach: 7.24×10^5 total compliance, 464 s, 53 iterations.

(b) Topology optimization: 7.26×10^5 total compliance, 197 s, 100 iterations.

Fig. 28. Comparisons between the optimized ETPMS-based porous structure and the structure obtained from traditional topology optimization for the multilayer table example in Fig. 16(c).

not readily derived and computed. Devising a more mature surrogate model; for example, based on the deep neutral network [23], may help to address this issue. Furthermore, extending the approach to include other types of microstructures and additional design variables, such as the rotation angle, may further improve its use and performance in industrial applications, and is currently under study. Finally, owing to the imposed constraints, the proposed ETPMS approach cannot yield a complete void microstructure at any mesh element, which may deteriorate the performance of the resulting porous structure. This topic will be explored in future work; for example, by introducing an additional density variable.

CRediT authorship contribution statement

Ming Li: Conceptualization, Methodology, Software, Visualization. **Liangchao Zhu:** Data curation, Software, Visualization. **Jingzhi Li:** Funding acquisition, Investigation, Methodology, Supervision, Writing - review & editing. **Kai Zhang:** Software, Validation, Writing - original draft, Writing - review & editing.

Declaration of competing interest

The authors declare that they have no known competing financial interests or personal relationships that could have appeared to influence the work reported in this paper.

Acknowledgements

The valuable comments from the anonymous reviewers are greatly appreciated. The work of M. Li is supported by the NSF of China (No. 61872320). The work of Li was partially supported by the NSF of China No. 11971221 and 11731006, the Shenzhen Sci-Tech Fund No. JCYJ20190809150413261 and JCYJ20170818153840322, and Guangdong Provincial Key Laboratory of Computational Science and Material Design No. 2019B030301001. The work of K. Zhang is supported by the NSF of China under the grant No. 11871245, and by the Key Laboratory of Symbolic Computation and Knowledge Engineering of Ministry of Education, Jilin University (93K172018Z01).

References

[1] N.A. Fleck, V.S. Deshpande, M.F. Ashby, Micro-architectured materials: past, present and future, Proc. R. Soc., Math. Phys. Eng. Sci. 466 (2121) (2010) 2495–2516.
[2] I. Elnasri, S. Pattofatto, H. Zhao, H. Tsitsiris, F. Hild, Y. Girard, Shock enhancement of cellular structures under impact loading: Part I Experiments, J. Mech. Phys. Solids 55 (12) (2007) 2652–2671.
[3] I.S. Golovin, H.R. Sinning, Damping in some cellular metallic materials, J. Alloys Compd. 355 (1) (2003) 2–9.
[4] E.W. Andrews, L.J. Gibson, The influence of cracks, notches and holes on the tensile strength of cellular solids, Acta Mater. 49 (15) (2001) 2975–2979.
[5] P. Fratzl, R. Weinkamer, Nature's hierarchical materials, Prog. Mater. Sci. 52 (8) (2007) 1263–1334.
[6] S. Gomez, M. Vlad, J. Lopez, E. Fernandez, Design and properties of 3D scaffolds for bone tissue engineering, Acta Biomater. 42 (2016) 341–350.
[7] M. Zhou, Y. Liu, Z. Lin, Topology optimization of thermal conductive support structures for laser additive manufacturing, Comput. Methods Appl. Mech. Eng. 353 (2019) 24–43.
[8] M.P. Bendsøe, N. Kikuchi, Generating optimal topologies in structural design using a homogenization method, Comput. Methods Appl. Mech. Eng. 71 (2) (1988) 197–224.
[9] H. Rodrigues, J. Guedes, M. Bendsøe, Hierarchical optimization of material and structure, Struct. Multidiscip. Optim. 24 (1) (2002) 1–10.
[10] G.H. Paulino, E.C.N. Silva, C.H. Le, Optimal design of periodic functionally graded composites with prescribed properties, Struct. Multidiscip. Optim. 38 (5) (2009) 469–489.

[11] L. Xia, P. Breitkopf, Concurrent topology optimization design of material and structure within FE2 nonlinear multiscale analysis framework, Comput. Methods Appl. Mech. Eng. 278 (2014) 524–542.
[12] J.P. Groen, J. Wu, O. Sigmund, Homogenization-based stiffness optimization and projection of 2D coated structures with orthotropic infill, Comput. Methods Appl. Mech. Eng. 349 (2019) 722–742.
[13] H. Zong, H. Liu, Q. Ma, Y. Tian, M. Zhou, M.Y. Wang, VCUT level set method for topology optimization of functionally graded cellular structures, Comput. Methods Appl. Mech. Eng. 354 (2019) 487–505.
[14] D. Li, W. Liao, N. Dai, Y.M. Xie, Anisotropic design and optimization of conformal gradient lattice structures, Comput. Aided Des. 119 (2020) 102787.
[15] F. Chinesta, P. Ladeveze, E. Cueto, A short review on model order reduction based on proper generalized decomposition, Arch. Comput. Methods Eng. 18 (4) (2011) 395.
[16] S. Besdo, Determination of dynamically adapting anisotropic material properties of bone under cyclic loading, J. Biomech. 44 (2) (2011) 272–276.
[17] S. Tawfick, M.D. Volder, D. Copic, S.J. Park, C.R. Oliver, E.S. Polsen, M.J. Roberts, A.J. Hart, Engineering of micro- and nanostructured surfaces with anisotropic geometries and properties, Adv. Mater. 24 (13) (2012) 1628–1674.
[18] X. Kou, S. Tan, A simple and effective geometric representation for irregular porous structure modeling, Comput. Aided Des. 42 (10) (2010) 930–941.
[19] S. Gómez, M. Vlad, J. López, E. Fernández, Design and properties of 3D scaffolds for bone tissue engineering, Acta Biomater. 42 (2016) 341–350.
[20] Y. Wang, Loci periodic surface reconstruction from crystals, Comput-Aided Des. Appl. 4 (1–4) (2007) 437–447.
[21] D.-J. Yoo, Heterogeneous porous scaffold design for tissue engineering using triply periodic minimal surfaces, Int. J. Precision Eng. Manufac. 13 (4) (2012) 527–537.
[22] H. Li, Z. Luo, L. Gao, P. Walker, Topology optimization for functionally graded cellular composites with metamaterials by level sets, Comput. Methods Appl. Mech. Eng. 328 (2018) 340–364.
[23] D.A. White, W.J. Arrighi, J. Kudo, S.E. Watts, Multiscale topology optimization using neural network surrogate models, Comput. Methods Appl. Mech. Eng. 346 (2019) 1118–1135.
[24] E. Garner, H.M. Kolken, C.C. Wang, A.A. Zadpoor, J. Wu, Compatibility in microstructural optimization for additive manufacturing, Additive Manufac. 26 (2019) 65–75.
[25] Z. Du, X.-Y. Zhou, R. Picelli, H.A. Kim, Connecting microstructures for multiscale topology optimization with connectivity index constraints, J. Mech. Des. 140 (11) (2018) 111417.
[26] X. Liu, V. Shapiro, Sample-based synthesis of two-scale structures with anisotropy, Comput. Aided Des. 90 (2017) 199–209.
[27] F. Regazzoni, N. Parolini, M. Verani, Topology optimization of multiple anisotropic materials, with application to self-assembling diblock copolymers, Comput. Methods Appl. Mech. Eng. 338 (2018) 562–596.
[28] A. Dumon, C. Allery, A. Ammar, Proper general decomposition (PGD) for the resolution of Navier–Stokes equations, J. Comput. Phys. 230 (4) (2011) 1387–1407.
[29] S. Zlotnik, P. Díez, D. Modesto, A. Huerta, Proper generalized decomposition of a geometrically parametrized heat problem with geophysical applications: PGD of a geometrically parametrized heat problem for geophysics, Int. J. Numer. Methods Eng. 103 (10) (2015) 737–758.
[30] L. Zhu, M. Li, R.R. Martin, Direct simulation for CAD models undergoing parametric modifications, Comput. Aided Des. 78 (2016) 3–13.
[31] R. Hill, Elastic properties of reinforced solids: some theoretical principles, J. Mech. Phys. Solids 11 (5) (1963) 357–372.
[32] B. Hassani, E. Hinton, A review of homogenization and topology optimization II - analytical and numerical solution of homogenization equations, Comput. Struct. 69 (6) (1998) 719–738.
[33] T.G. Kolda, B.W. Bader, Tensor decompositions and applications, SIAM Rev. 51 (3) (2009) 455–500.
[34] K. Svanberg, The method of moving asymptotes – a new method for structural optimization, Int. J. Numer. Methods Eng. 24 (2) (1987) 359–373.
[35] C. Zillober, A globally convergent version of the method of moving asymptotes, Struct. Optim. 6 (3) (1993) 166–174.
[36] M.P. Bendsoe, O. Sigmund, Topology Optimization: Theory, Methods and Applications, Springer, 2003.
[37] O. Sigmund, S. Torquato, Design of materials with extreme thermal expansion using a three-phase topology optimization method, J. Mech. Phys. Solids 45 (6) (1997) 1037–1067.
[38] K. Liu, A. Tovar, An efficient 3D topology optimization code written in Matlab, Struct. Multidiscip. Optim. 50 (6) (2014) 1175–1196.